Journal of Hydrology 677 (2026) 135780

Contents lists available at ScienceDirect

Journal of Hydrology

journal homepage: www.elsevier.com/locate/jhydrol

Research papers

Refining image-based approaches for river monitoring: a focus on graphical enhancement and software parameter sensitivity

Francesco Alongi [a,*], Robert Ljubičić [b], Silvano Fortunato Dal Sasso [c], Leonardo Valerio Noto [a]

[a] Department of Engineering, University of Palermo, Palermo, Italy
[b] Department of Hydraulic and Environmental Engineering, Faculty of Civil Engineering, University of Belgrade, Belgrade, Serbia
[c] Department for Humanistic, Scientific, and Social Innovation, University of Basilicata, Matera, Italy

A R T I C L E I N F O

This manuscript was handled by Marco Borga, Editor-in-Chief, with the assistance of George Constantinescu, Associate Editor

Keywords:
LSPIV
Surface velocity estimation
Graphical enhancement filters
Optical flow
PIVlab
SSIMS-flow
River monitoring

A B S T R A C T

Image-based techniques for estimating river surface velocity include traditional Large-Scale Particle Image Velocimetry (LSPIV), which infers tracer displacement by computing cross-correlation between pairs of consecutive frames, and optical flow approaches, which derive motion from image intensity gradients. Their accuracy strongly depends on image quality and processing configurations. However, the influence of enhancement techniques and parameter settings on large-scale velocimetry has not yet been systematically explored, due to complex interactions between field conditions, enhancement methods, and software-specific options. As a result, most studies still rely on authors' experience and the processing tools available in the selected software. This study presents a sensitivity analysis evaluating the impact of different combinations of graphical enhancement filters and software parameterizations under varying environmental conditions. Image-based measurements were performed in two case studies in Sicily (Italy): the Oreto and Platani rivers. Acquired videos were pre-processed applying enhancement filters and multiple parameter configurations were tested. Analyses were performed using PIVlab and SSIMS-Flow, each tested with distinct processing setups. Overall, 1296 surface velocity fields were derived and compared to ADCP reference data. Water clarity and background complexity were objectively quantified using the Normalized Difference Turbidity Index (NDTI). Results demonstrate that both filter selection and software settings significantly influence image velocimetry accuracy. PIVlab, relying on cross-correlation, showed greater robustness in visually complex scenarios, while SSIMS-Flow, based on intensity gradients, achieved higher accuracy in uniform and turbid conditions. Poor performance generally corresponded to unsuitable filter-parameter combinations. Overall, the proposed framework helps refine image-based velocimetry workflows for more accurate field implementations.

1. Introduction

River monitoring is a fundamental activity in hydrological studies (Depetris, 2021), providing crucial data for water resource management (Ellison et al., 2019; Anwar Sadat et al., 2020; Shanafield et al., 2021), flood prediction (Merkuryeva et al., 2015; Munawar et al., 2022) and risk assessment (Winsemius et al., 2013; Camarasa-Belmonte, 2021), and for understanding river system dynamics (Langat et al., 2019; Zhao et al., 2023). Monitoring the hydrological regime involves real-time measurements of hydrometric level, discharge, and flow velocity at key sections. Hydrometric level (also known as stage) is typically measured at fixed gauge stations using float-operated, pressure, or radar devices. Discharge is typically estimated through rating curves, which relate stage to discharge. These curves are established using measurements of flow velocity and cross-sectional area obtained with current meters, acoustic Doppler devices, or tracer-based methods. Building accurate rating curves requires repeated discharge measurements across a wide range of conditions, including flood events (Smart, 1992; Abril and Knight, 2004; Birgand et al., 2013; Muste and Hoitink, 2017). However, extreme events are difficult to monitor due to safety risks and logistical constraints (e.g., strong currents, floating debris, unstable riverbanks). As a result, extrapolations are often necessary, increasing

* Corresponding author.
E-mail addresses: francesco.alongi01@unipa.it (F. Alongi), rljubicic@grf.bg.ac.rs (R. Ljubičić), silvano.dalsasso@unibas.it (S.F. Dal Sasso), leonardo.noto@unipa.it (L.V. Noto).

https://doi.org/10.1016/j.jhydrol.2026.135780
Received 26 August 2025; Received in revised form 13 May 2026; Accepted 27 May 2026
Available online 27 May 2026

uncertainty and potential errors (Sivapragasam and Muttil, 2005; Guven et al., 2013; McMahon and Peel, 2019). Instrument limitations and assumptions about flow uniformity may also lead to inaccuracies, especially in turbulent or non-typical conditions.

Technological advances have significantly enhanced monitoring capabilities (Manfreda et al., 2018; Tauro et al., 2018; Acharya et al., 2021; Mihel et al., 2024). Modern systems integrate in-situ sensors, remote sensing, and satellite imagery to provide accurate, real-time data and support rapid responses to natural or anthropogenic changes. Remote sensing enables large-scale river observation, even in inaccessible areas (Piégay et al., 2020; Wei et al., 2021), while unmanned aerial vehicles (UAVs, drones) enhance river mapping through low-altitude photogrammetry (Iqbal et al., 2023) and 3D modeling (Gracchi et al., 2021; Yan et al., 2023).

To overcome the limitations of traditional river monitoring, optical-based velocimetry techniques are being increasingly adopted for their ability to provide high-resolution, non-intrusive measurements, even under complex flow conditions (Dal Sasso et al., 2021a; Peña-Haro et al., 2021; Bodart et al., 2022; Koutalakis and Zaimes, 2022; Chen et al., 2024; Manfreda et al., 2024). These methods employ image processing techniques to track the movement of surface tracers or natural flow patterns, estimating surface velocity fields over time. Their non-intrusive nature enhances safety and flexibility, allowing remote observations over large areas with lower cost and maintenance compared to conventional tools. Among the most widely used techniques, Large-Scale Particle Image Velocimetry (LSPIV) (Fujita et al., 1998; Meselhe et al., 2004; Muste et al., 2008) and Large-Scale Particle Tracking Velocimetry (LSPTV) (Tang et al., 2008; Tauro et al., 2019) have gained particular prominence. LSPIV uses cross-correlation algorithms to estimate average surface flow fields, adopting a Eulerian approach that analyzes the flow at fixed locations. It has proven effective even in challenging environments with variable lighting and complex flows (Creutin et al., 2003; Le Coz et al., 2010; Dramais et al., 2011; Kantoush et al., 2011; Ran et al., 2016). LSPTV, in contrast, follows individual tracers through a Lagrangian approach, providing a more detailed velocity reconstruction (Admiraal et al., 2004; Rosero Legarda et al., 2022). A more recent alternative is the optical flow method, which estimates motion by tracking changes in pixel intensity between consecutive frames, under the assumption of the brightness constancy constraint (Farnebäck, 2003). Unlike LSPIV and LSPTV, it can often operate with fewer visible tracers.

The application of image-based velocimetry techniques follows a structured workflow, including data acquisition, image processing, velocity estimation, and final analysis (Jolley et al., 2021). High-quality video sequences of the water surface are captured using fixed cameras, UAVs, or handheld devices, depending on site conditions and required resolution. The footage then undergoes a pre-processing phase to improve image quality for accurate velocity estimation. Pre-processing may involve stabilization to correct unwanted camera movements, especially with UAV or handheld recordings, followed by orthorectification to correct perspective distortions and convert pixel-based velocities to real-world units (Ljubičić et al., 2021). This step uses Ground Control Points, GCPs, for accurate spatial referencing. Graphical enhancement techniques can also be applied to increase the visibility of surface features. Tracer displacement is then analyzed using image-processing algorithms implemented to estimate surface velocities. Post-processing includes filtering and interpolation to remove outliers and fill data gaps. The final velocity fields can support various hydrodynamic applications, including discharge estimation (Kumar Vyas et al., 2024; Pumo et al., 2025).

Despite their advantages, image-based velocimetry techniques are not yet widely adopted. Unlike traditional methods, which follow standardized protocols, these innovative approaches lack specific regulatory frameworks (Pumo et al., 2021), making it necessary to rely on best practices, field experience, and ongoing research to reduce errors and improve accuracy. A key prerequisite for making reliable measurements is the presence of visible tracers or natural water surface features, which is particularly critical in situations where adding material is not feasible. Even in cases where artificial materials can be introduced, insufficient or uneven tracer seeding can compromise the spatial and temporal representativeness of the derived velocity fields (Ljubičić et al., 2024). Several other factors can influence optical measurements. Low resolution video can lead to missed or misidentified tracers, resulting in inaccurate flow velocity calculations (Liu et al., 2021). Camera stability is also essential, as even minor vibrations or shifts can distort tracking results (Lewis and Rhoads, 2018; Ljubičić et al., 2021). Environmental and hydraulic conditions (e.g., fluctuating lighting, waves, turbulence, debris) can degrade image quality and hinder feature recognition (Fujita et al., 2020; Mohajeri et al., 2024). Oblique viewing angles can introduce geometric distortions (Le Coz et al., 2021), while image processing algorithms may be affected by background noise, compression artifacts, or suboptimal parameter settings.

Many recording-related errors can be minimized through careful planning and best practices. Proper camera placement, stable mounting, and optimal viewing angles are essential to prevent vibrations and ensure high-quality recordings. However, environmental and hydraulic factors during video acquisition are harder to control. In such cases, enhancing the informative content of the footage becomes important. Similarly, when tracers are manually introduced, ensuring a uniform and dense distribution improves motion detection and velocity estimates. If consistent seeding cannot be guaranteed, it is advisable to analyze only video segments with optimal tracer conditions (Pizarro et al., 2020a, 2020b; Dal Sasso et al., 2021a; Alongi et al., 2023).

Even with best practices in the field, uncertainty in optical-based velocimetry often arises from the graphical enhancement of recorded images and the parameterization of the software used to evaluate surface velocity fields (Zhang et al., 2013; Chen et al., 2024). Enhancing tracers' visibility against the background is crucial for accurate motion detection, but its effectiveness depends on environmental conditions at the time of recording and tracer characteristics. Likewise, the choice of software parameters plays a fundamental role in extracting reliable velocity vectors from processed images. The software parameters must be optimized based on the resolution of the video and the expected velocity range (Liu et al., 2021; Bodart et al., 2022; Wijaya et al., 2023; Legleiter and Kinzel, 2024a; Mohajeri et al., 2024). However, some of the most influential sources of uncertainty originate during data acquisition and cannot be fully corrected during post-processing. The flying height or camera distance from the water surface determines the ground sampling distance (i.e., pixel size), which controls the spatial resolution and the minimum detectable tracer displacement. Similarly, the capture interval, defined by the video frame rate, must be selected according to the expected flow velocity to ensure measurable particle displacements without excessive advection between frames, which can lead to decorrelation or particle loss. In cross-correlation-based methods, selecting the appropriate interrogation area size affects the resolution and reliability of the velocity field (Giannopoulos et al., 2022). These parameters must be considered along with pixel size and frame interval to maintain tracer displacement within a range suitable for robust correlation, typically not exceeding about half of the interrogation area. If the interrogation window is too large, the algorithm can miss small-scale movements, while small windows can increase noise and reduce correlation robustness (Legleiter and Kinzel, 2024b). Similarly, in optical flow algorithms, parameters related to the motion scale or temporal resolution can drastically affect outcomes, especially in turbulent flows (Ljubičić et al., 2024). All these considerations are particularly relevant for UAV-based river imagery, where tools like TRiVIA's Tool for Input Parameter Selection (TIPS) provide guidance of optimizing settings for site-specific conditions (Legleiter and Kinzel, 2024b).

Despite the growing application of image-based velocimetry, the role of image enhancement techniques in optimizing surface velocity estimation remains insufficiently investigated. Most studies focus on the core processing algorithms, whereas image pre-processing operations such as contrast enhancement, noise reduction, or background subtraction, are often applied in an *ad hoc* manner, without standardized criteria or quantitative assessment. Yet, the visibility and distinguishability of surface tracers are critical for the reliability of motion tracking algorithms. Previous research has shown that image enhancement can significantly influence tracer detectability and, consequently, the accuracy of velocity estimates (Zhang et al., 2013; Bodart et al., 2022). When appropriately tailored to flow and image conditions, different filters can substantially improve tracer contrast, suppress background noise, and increase pattern definition, particularly under challenging conditions such as those characterized by turbulence, debris, strong reflections, or low contrast (Strelnikova et al., 2023). While related aspects such as the role of seeding characteristics or automated frame selection for optimal analysis (Dal Sasso et al., 2021b; Alongi et al., 2023) have been addressed, a systematic evaluation of enhancement filters and their interaction with software parameterization is still lacking. This study addresses that gap by assessing how different enhancement techniques, in combination with LSPIV and optical flow configuration settings, influence performance across diverse environmental scenarios.

This work presents a detailed sensitivity analysis of image velocimetry techniques, focusing on two critical workflow stages: (a) graphical enhancement during pre-processing and (b) parameter selection during velocity inference. The analysis is based on measurements from two rivers in Sicily (Italy), collected during a discharge measurement campaign carried out between 2020 and 2021. Field data were acquired along specific transects using a traditional ADCP, providing benchmark velocities and the corresponding discharges, and an LSPIV setup, which involved tracer dispersion on the water surface and video recording from both a fixed camera and a drone. To evaluate how image quality influences the LSPIV performance, each measurement was characterized in terms of water clarity and visual background complexity using the Normalized Difference Turbidity Index (NDTI, Lacaux et al., 2007) as an indicator of turbidity and contrast variability in the images. This allowed us to distinguish between conditions with relatively uniform backgrounds and others with high visual noise. A range of image-based velocimetry software tools is currently available for surface flow monitoring, including both general-purpose particle image velocimetry implementations and platforms specifically designed for river environments. River-oriented tools often provide dedicated workflows that integrate image stabilization, parameter selection support, and accuracy assessment, as well as processing strategies tailored to natural channel conditions (Legleiter, 2023; Legleiter and Kinzel, 2023, 2024b). Other approaches, such as KLT-IV (Perks, 2020), HydroSTIV (Watanabe et al., 2021), and many others, further expand the range of available methods for estimating surface velocities in natural flows. Within this broad landscape, the present study focuses on two representative tools with different computational foundations. PIVlab (Thielicke and Stamhuis, 2014) was selected as a widely recognized and extensively used implementation of traditional PIV principles, while SSIMS-Flow (Ljubičić et al., 2024) represents a newer software based on optical flow method for motion estimation. Understanding of how image enhancement choices and parameter configurations affect the final velocity estimates remains incomplete. Both our own field experience and the insights of leading researchers in image-based hydrodynamics indicate that the influence of pre-processing choices on velocimetry outputs is often underappreciated. Advancing the understanding of the influence of pre-processing, is not only relevant as a research challenge but is also highly valuable for practicing engineers who rely on robust, repeatable surface velocity measurements for hydrometric applications. For this reason, this study explicitly aims to clarify the role of image enhancement and software parameterization by systematically testing their effects across a set of environmental scenarios. By comparing these tools under varying enhancement and parameterization conditions, this work aims to provide a deeper understanding of how different computational approaches respond to changes in image quality and processing settings.

2. Materials and methods

2.1. Field case studies

The analyses were conducted considering two case studies: the Oreto (OR) and the Platani (PL) rivers, both located in Sicily (Southern Italy). The OR river flows in the northwestern part of the island, whereas the PL river crosses central Sicily before flowing into the Mediterranean Sea. Both case studies were part of a broader discharge measurement campaign carried out across the region between 2020 and 2021 (Fig. 1).

At the investigated cross-sections, the OR drains approximately 70 km^2, with a mean annual discharge of 0.65–0.70 m^3/s, while the PL has a much larger basin ($\sim$1220 km^2) and an average annual discharge between 1.5 and 2.0 m^3/s. The two rivers differ primarily in channel morphology. The OR is characterized by a natural sandy riverbed and gabion-lined banks for stability, especially during floods. Visual inspection during the measurement campaigns did not reveal any evidence of bedform migration or sediment motion, and the riverbed appeared stable over the duration of the measurement activities. The OR channel width ranges from $\sim$10 m under ordinary flow to $\sim$20 m during high-flow events. In contrast, the PL features an artificial concrete riverbed with a trapezoidal cross-section: the low-flow section is circular ($\sim$5 m wide), expanding to 15–20 m over side benches, and up to nearly 100 m under flood conditions. Both sites were subjected to multiple image-based measurements over time (i.e., three measurements per case study). Benchmark data were simultaneously collected using ADCP (Table 1).

Image-based measurements were performed by dispersing a commercially available and low-cost tracer on the water surface (i.e., wooden chips with an average size of $\sim$35 mm), chosen for its environmental sustainability, non-toxicity, and good visual contrast against background. Tracers were manually dispersed from the riverbanks to ensure uniform coverage and adequate density over the area of interest. For the OR, video recordings were made through a fixed camera (i.e., Nikon Coolpix P530 – 1920x1080, 25 fps) mounted on a tripod above a bridge; for the PL, recordings were acquired with a drone (i.e., DJI Mavic – 1920x1080, 30 fps), equipped with a full HD camera. Marker panels, consisting of black-and-white checkerboards, were placed within the scene served as Ground Control Points (GCPs) for video stabilization and orthorectification, with coordinates obtained via a high-precision GNSS receiver (Stonex S500 GNSS). Recordings captured a variety of environmental and hydraulic conditions. While sunny weather offered good illumination, shadows and lighting variability occasionally introduced visual challenges. For the OR, low sediment concentrations made the riverbed visible under sunlight, introducing background noise in the recorded frames. In contrast, for the PL recordings, a higher sediment concentration prevented disturbances from the riverbed. ADCP measurements were conducted following the World Meteorological Organization (WMO) standards and the United States Geological Survey (USGS) guidelines using a StreamPro ADCP produced by Teledyne RD Instruments (TRDI). Measurements were taken along a transect within the LSPIV recording area. Since StreamPro ADCP cannot sample the uppermost portion of the water columns due to the submersion of the sensor, the procedure described in Alongi et al. (2023) was applied to obtain reliable surface velocity benchmarks for comparison with LSPIV measurements.

2.2. Characterization of water clarity conditions

Since image-based velocimetry relies on distinguishing tracers from the background, the optical contrast between the water surface and tracers affects velocity estimation accuracy. To characterize water clarity during each LSPIV acquisition, the Normalized Difference Turbidity Index (NDTI; Lacaux et al., 2007) was used, a remote sensing-

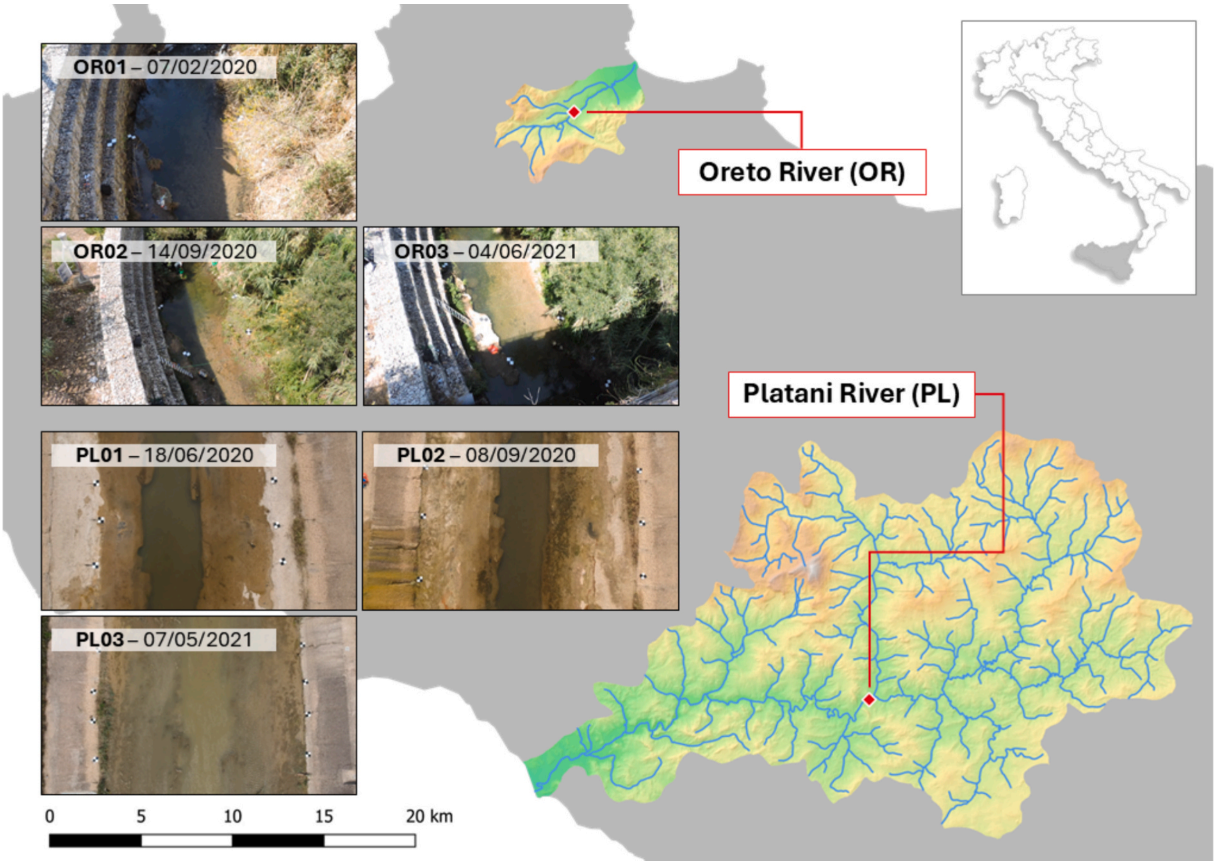

Fig. 1. The monitored rivers, Oreto (OR) and Platani (PL), are marked with red dots at their respective measurement sites. Watersheds and river networks (blue lines) are also highlighted. Images illustrate multiple measurements performed at each site on different dates. (For interpretation of the references to colour in this figure legend, the reader is referred to the web version of this article.)

Table 1
Summary of ADCP and image-based measurements conducted on the Oreto (OR) and Platani (PL) rivers. For each case study, three measurement sessions are reported with date, depth-averaged velocity (V_{avg}), and discharge (Q) from ADCP measurements. LSPIV acquisition details are also included: acquisition mode, acquisition frame rate (fps), and spatial resolution. Additionally, the Normalized Difference Turbidity Index (NDTI) is reported through its average ($NDTI_{avg}$) and standard deviation ($NDTI_{std}$) values, providing a characterization of water clarity and visual background complexity for each measurement.

ID		Date	ADCP measurement			Image-based measurement			
			V_{avg}	Q	Acquisition mode	Acquisition frame rate	Spatial resolution	$NDTI_{avg}$	$NDTI_{std}$
			m/s	*m³/s*	–	*fps*	*m/px*	–	–
OR	**01**	**07/02/2020**	0.08	0.30	bridge	25	0.0108	−0.146	0.163
	02	**14/09/2020**	0.05	0.16	bridge	25	0.0099	0.005	0.145
	03	**04/06/2021**	0.08	0.22	bridge	25	0.0101	0.058	0.063
PL	**01**	**18/06/2020**	0.15	0.23	drone	30	0.0099	0.154	0.023
	02	**08/09/2020**	0.19	0.32	drone	30	0.0100	0.160	0.030
	03	**07/05/2021**	0.20	0.63	drone	30	0.0100	0.101	0.011

based index widely applied in water quality studies (Rawat et al., 2023; Xu et al., 2023; Dabire et al., 2024; Singh et al., 2024). NDTI is defined as in Eq. (1):

$$NDTI = \frac{\rho_{red} - \rho_{green}}{\rho_{red} + \rho_{green}} [-] \tag{1}$$

where ρ_{red} and ρ_{green} are the reflectance values in the red and green bands, respectively.

Theoretical NDTI values range between −1 and + 1, though typical values over inland/coastal waters fall between −0.25 and + 0.25 (Rawat et al., 2023). Higher NDTI values generally indicate increased turbidity, due to red-band backscattering by suspended particles; lower values suggest clearer water dominated by green-band reflectance.

Although NDTI is typically applied to multispectral satellite or airborne imagery, in this study it was computed from RGB (i.e., red–green–blue) video frames acquired during image-based measurements using standard digital cameras. A specific procedure of reflectance calibration, developed to obtain NDTI from RGB video, is detailed in the supplementary material.

NDTI was calculated within a region of interest (ROI) in the watercourses, excluding riverbanks, vegetation, shadows, and sun glint, to ensure that the index reflected the actual optical quality of water. The average NDTI values (Table 1) thus obtained confirm a clear distinction between clear and turbid water conditions. In the OR cases, characterized by transparent water and visible riverbed (Fig. 1), NDTI ranged from −0.146 (OR01) to 0.058 (OR03), indicating higher green than red band reflectance, consistent with minimal suspended particles. In contrast, the PL cases, where the riverbed was not visible (Fig. 1), showed higher average NDTI values, from 0.100 (PL03) to 0.160 (PL02), reflecting increased red band reflectance typically associated with turbidity. The standard deviation of NDTI (Table 1) offers further insight into spatial variability. The OR cases exhibited higher variability (up to 0.163 in OR01), likely due to the heterogeneity from visible riverbed features. Conversely, the PL cases showed lower $NDTI_{std}$ values, suggesting more uniform optical conditions.

2.3. Preliminary processing of video sequences

During the experiments, flow velocities were relatively low, often resulting in "sub-pixel" displacements which are tracer movements between frames smaller than a single pixel, due to an acquisition frame rate excessively high in relation to flow velocity. To mitigate this issue, the acquired videos were downsampled considering an operational frame rate equal to half of the acquisition one (i.e., from 25 to 12.5 fps for the OR measurements, from 30 to 15 fps for the PL measurements). Subsequently, the sequences underwent stabilization to remove camera movements unrelated to tracer motion, and orthorectification to correct perspective distortions using GCPs coordinates. Both pre-processing steps were performed using the SSIMS-Flow software, a versatile and highly efficient solution for such operations. Once stabilized and orthorectified, the optimal sub-sequence for analysis was selected following the methodology proposed by Alongi et al. (2023). From each original sequence (>5 min), the best 120-second sub-sequence was extracted, ensuring adequate tracer coverage over the recorded area and reducing the computational time required for the subsequent analyses.

2.4. Graphical enhancement filters

As highlighted in the previous section, graphical enhancement is a critical step that significantly affects the performance of optical velocimetry techniques. Its goal is to increase contrast between tracers and background, and the choice of filters strongly depends on environmental and hydraulic conditions. Various factors, including lighting, turbidity, and flow complexity, require tailored strategies to ensure optimal image clarity. In well-lit scenes, where tracers are generally clearly visible, simple filters such as contrast stretching or basic edge detection, may be sufficient. Under low-light conditions, more advanced techniques like color histogram equalization may be needed to amplify tracer visibility. Surface reflections (e.g., sun glint) can hinder analysis; in such cases, contrast-enhancing filters that suppress high-frequency noise help to reduce reflections while preserving tracer detail.

In this study, a variety of graphical enhancement filters were explored, from widely used traditional filters to less common ones. SSIMS-Flow was used at this stage for its wide assortment of filters and the capability to apply them in a "stacked" mode, allowing one or multiple filters to be applied sequentially in a desired order. The filters investigated were grouped into three categories: (i) traditional, (ii) edge-detection, and (iii) background removal.

Among the traditional filters, the greyscale transformation ("GRAY") was considered. In standard workflows, greyscale information is generally exploited during stabilization, which is performed on single-channel data, while orthorectification is carried out on the full multi-channel images to preserve valuable information. The transformation to greyscale may then be applied subsequently, after rectification. GRAY is particularly effective in scenarios where the natural colour of tracers blends with the environment, such as when sediment or other in-water elements generate a complex background. In such cases, the contrast in grey intensity between tracers and surroundings becomes more pronounced. After the application of GRAY, additional traditional filters were individually tested in a stacked configuration: intensity capping ("CAP"), the high-pass filter ("HPASS"), and the Contrast Limited Adaptive Histogram Equalization (CLAHE – "HIST") algorithm.

- The CAP constrains pixel intensity within a specified range, preventing the impact of overly bright areas (e.g., reflections, glare, sun glint). The capping threshold is defined as a number (N) of standard deviations of image-average pixel intensities from the image median intensity.
- The HPASS filter emphasizes sharp details and edges by suppressing low-frequency components. This is achieved by applying a Gaussian blur, which is a low-pass filter, and subtracting the result from the original image. The method relies on a single parameter, the blur strength (σ), which controls the degree of low-frequency suppression.
- The HIST filter is based on CLAHE algorithm, which improves local contrast while limiting noise amplification. Unlike traditional histogram equalization, CLAHE operates on small, localized regions (i.e., tiles) of the image, making it effective under uneven lighting conditions. It requires two parameters: the clip value (c), which limits contrast amplification, and the tile size (t_s), which defines the dimension of local regions for equalization. This localized approach enhances visibility in shadowed or overexposed areas without distorting the rest of the image.

Among the edge-detection filters not included in traditional velocimetry software, two algorithms were investigated in this study: the Sobel detector and the Canny Detector, both applied after GRAY transformation.

- The Sobel detector ("EDGE1") is a differential operator that computes brightness gradients in the image, identifying the direction with the maximum pixel intensity gradient and measuring the rate of change along that direction. The resulting output provides an estimate of how sharply or gradually the intensity changes at each point. The Sobel operator applies two convolution kernels to approximate derivatives in horizontal and vertical directions. The kernel size (k_s) is a key parameter influencing sensitivity to edge detail.
- The Canny detector ("EDGE2") applies a multi-stage process. First, the image is blurred using a Gaussian filter to reduce noise. Then, gradients are calculated in multiple directions (horizontal, vertical, and diagonal), and the direction with the highest gradient is selected for each pixel. The resulting gradient map is processed using "hysteresis thresholding", based on two thresholds: a lower (τ_{low}) and an upper (τ_{up}) one. Pixels with gradient below τ_{low} are discarded, while pixels with gradient exceeds τ_{up} are accepted as edges. If the gradient value falls between τ_{low} and τ_{up}, pixels are accepted only if they are connected to an accepted edge. The final output is a binary image identifying edge pixels.

The last category of filters, typically absent in traditional optical software, involves background removal. This process identifies static, non-moving elements, the so-called background, and isolates tracer particles, the foreground, by subtracting the background from each frame. For reliable results, background objects must remain stationary in the image sequence, meaning that image stabilization is essential before background subtraction. The background can be estimated by calculating the median pixel value over a set of stabilized frames (n_f). Two approaches were investigated:

- BACK1: traditional background subtraction based on greyscale images, where n_f frames are used to identify the background;
- BACK2: background subtraction using n_f RGB images, with the color channels selected based on prior visual inspection of the individual RGB channels from the original frames, retaining the one that provided the clearest tracer-background differentiation.

Each enhancement filter tested in this study is governed by specific parameters that influence how tracers are visually emphasized. To assess their impact, five different parameter configurations were applied for each filter, except GRAY, which simply converts images to single-channel format and does not require user-defined settings (Table 2).

The parameter values for each filter were selected to explore different levels of enhancement and suppression under varying conditions. For each adjustable parameter, Table 2 reports minimum and maximum values that define the full range of potentially admissible settings, or minimal and maximal values permitted by the SSIMS-Flow software. However, only a limited number of representative configurations (a-e) were actually tested within this range to evaluate filter performance under progressively varying processing intensity. In some cases, specific parameters were held constant at a single trade-off value, even though a broader range is theoretically possible. In addition, while certain methods exhibit linear parameter sensitivity, some behave according to an exponential progression. For CAP, negative values for N (CAP$^{(a)(b)}$) limit extreme intensities, useful in the presence of glare or reflections; positive values (CAP$^{(d)(e)}$) can enhance tracer visibility by emphasizing their contrast with the background. For HPASS, the blur strength σ was varied from low (HPASS$^{(a)}$ – minimal smoothing and detail preservation) to high (HPASS$^{(e)}$ – strong smoothing and enhanced edge definition). Lower values are expected to preserve more detail in the images, while as the values of σ increase, more of the low-frequency content is removed and the high-frequency components (i.e., sharp edges and small structures) are accentuated. For the HIST filter, low clip values c (HIST$^{(a)}$) yield stronger contrast enhancement, while higher values (HIST$^{(e)}$) produce less pronounced improvement. The tile size (t_s), although theoretically variable, was fixed at 32 in all configurations as a compromise between local sensitivity and global stability. Considering the Sobel detector, small kernel sizes (EDGE1$^{(a)(b)}$) detect fine details and thin edges but are more noise sensitive. Larger k_s sizes (EDGE1$^{(d)(e)}$) reduce noise and only highlight spatially prominent features. In the case of EDGE2, the lower threshold (τ_{low}) varied from permissive (EDGE2$^{(a)}$, sensitive to weak edges) to strict (EDGE2$^{(e)}$, capturing only strong gradients). The upper threshold (τ_{up}) was fixed at 200 across all configurations to isolate the influence of τ_{low}, which is typically the more sensitive Canny detector parameter (Choi and Ha, 2021). In background removal filters, different levels of background stability were tested by varying the number of frames n_f used. BACK1$^{(a)}$ and BACK2$^{(a)}$ consider a very short averaging window, while the most conservative choice, generating a highly stable background model, is given by BACK1$^{(e)}$ and BACK2$^{(e)}$. BACK1 is computationally simpler and less affected by color variation. BACK2 offers better performance when tracers differ chromatically from the background. In Fig. 2, an example of the visual results obtained for each filter and the corresponding parameter setting is presented.

A detailed comparison of the computational cost associated with each enhancement filter and their parameter configuration is provided in the supplementary material, together with normalized processing times and implementation notes.

2.5. Software parameterization

Another critical aspect influencing the accuracy of image velocimetry estimates is the selection of software processing parameters, which determine how tracer motion is identified and translated into velocity vectors. Some parameters have a more significant influence than others, as they control key aspects such as spatial resolution, noise reduction, and vector displacement coherence.

In this study, two different software tools were used: PIVlab and SSIMS-Flow, each based on distinct computational approaches. PIVlab relies on cross-correlation, offering both Direct Cross-Correlation (D-CC) and Fast Fourier Transform Cross-Correlation (FFT-CC). The latter was preferred for its computational efficiency (Pumo et al., 2021; Alongi et al., 2023). Velocity estimation is performed by tracking tracer displacement within an interrogation area (IA), whose size directly affects the resolution and accuracy of the results, as well as the range of detectable velocities (Legleiter and Kinzel, 2024a). In the FFT-CC mode, multi-pass processing allows the user to progressively refine the IA size, from large (coarse estimate) to small (fine detail) (Pumo et al., 2021). SSIMS-Flow, in contrast, estimates surface velocities based on color intensity gradients between frames, processing data at a pixel level. This results in very dense velocity fields, which are filtered in SSIMS-Flow using a spatial pooling technique to reduce the output size. The image is divided into N_bxN_b blocks, and within each block, only velocity vectors exceeding the block-specific mean magnitude are retained. This locally adaptive thresholding suppresses weak or spurious vectors typically associated with noise or low correlation quality, while preserving the dominant and spatially coherent motion within each region. The block size (N_b) is a user-defined parameter, which, like the IA in PIVlab, influences the final spatial resolution of velocity field. Larger blocks reduce noise but smooth out local velocity variations, while smaller blocks preserve local details but increase sensitivity to noise. Detailed explanation on the SSIMS-Flow algorithms can be found in literature (Ljubičić et al., 2024).

To systematically assess the effect of processing parameters on velocity estimation, three different configurations were tested for both software tools (Table 3). For PIVlab, IA sizes varied across the FFT-CC multi-pass approach, progressively refining spatial resolution across successive passes. For SSIMS-Flow, the effect of parameter variation was evaluated by altering the block size used in the spatial pooling process.

In PIVlab, the transition from IA$_1$ to IA$_4$ controls the resolution of the computational grid. As the IA size decreases across passes, the velocity field becomes increasingly detailed. In Ω_1^{P}, the initial IA$_1$ of 256 px provides a coarse grid that smooths out local variations but improves robustness, particularly in low-seeding conditions. The successive reduction in the IA size allows the software to refine the velocity field, increasing its spatial detail. In contrast, Ω_3^{P}, which uses smaller IAs, yields a denser grid and higher spatial resolution, though at the cost of increased sensitivity to noise and outliers. PIVlab assigns velocity

Table 2
Overview of the graphical enhancement filters applied in this study, grouped into three categories: traditional, edge-detection, and background removal. Each filter is characterized by specific parameters (Par). The minimum (min) and maximum (max) values define the full admissible range of each parameter, whereas only five representative configurations (a – e) were actually tested within this range. The GRAY filter has no adjustable settings.

Class	Name	Description	Par	min	max	Configurations				
						(a)	*(b)*	*(c)*	*(d)*	*(e)*
Traditional	**GRAY**	*Greyscale transformation*	–	–	–			–		
	CAP	*Intensity Capping filter*	N	−1	1	−1	−0.5	0	0.5	1
	HPASS	*High-pass filter*	σ	0.1	21	1	5	10	15	20
	HIST	*CLAHE algorithm*	c	0.1	10	0.5	2	4	6	10
			t_s	4	64			32		
Edge-detection	**EDGE1**	*Sobel detector*	k_s	3	31	3	9	17	25	31
	EDGE2	*Canny detector*	τ_{low}	1	255	50	100	150	200	250
			τ_{up}	1	255			200		
Background removal	**BACK1**	*Greyscale subtraction*	n_f	1	100	5	10	25	50	100
	BACK2	*RGB subtraction*	n_f	1	100	5	10	25	50	100

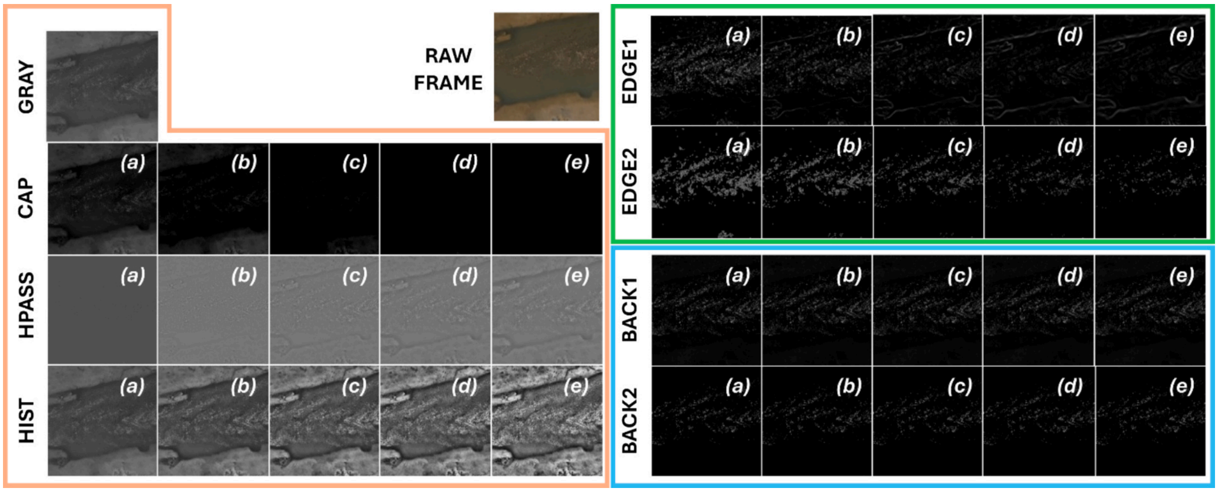

Fig. 2. Visual effects of the applied filters and their parameter configurations on a selected video frame from case study PL01, chosen for its optimal tracer density and distribution. The original RGB frame is shown at the top. Filters are grouped by categories: traditional (orange box), edge-detection (green box), and background removal (blue box). Each row corresponds to a specific filter, and columns represent the five parameter configurations (a–e). The GRAY filter is also shown in its single configuration, as it does not have adjustable parameters. Images are displayed as direct outputs of each filter configuration, without additional adjustments (e. g., histogram stretching or binarization), to represent the intrinsic visual effect of each filter. Consequently, some parameter configurations produce strong signal attenuation and appear very dark. (For interpretation of the references to colour in this figure legend, the reader is referred to the web version of this article.)

Table 3
Processing parameter configurations for PIVlab and SSIMS-Flow. In PIVlab, three multi-pass schemes were tested, with IA sizes progressively reduced across four passes. In SSIMS-Flow, three spatial pooling configurations were evaluated by varying the block size (N_b) used to aggregate velocity data.

PIVlab	Software Setup	IA_1	IA_2	IA_3	IA_4	SSIMS-Flow	Software Setup	N_b
		px	*px*	*px*	*px*			*px*
	Ω_1^P	256	128	64	32		Ω_1^S	16
	Ω_2^P	128	64	32	16		Ω_2^S	32
	Ω_3^P	64	32	16	8		Ω_3^S	64

vectors to the nodes of a regular, equidistant grid, with spacing directly dependent on IAs sizes; intermediate values are typically interpolated. SSIMS-Flow, by contrast, computes velocity directly at the pixel level, wherever valid tracer motion is detected, without a predefined grid. In configuration Ω_1^S, the smallest pooling block N_b offers the highest resolution but is more prone to data sparsity and noise. The intermediate configuration Ω_2^S balances resolution and noise reduction, improving stability while preserving local detail. The largest pooling block size ($N_b = 64px, \Omega_3^S$), provides the most stable but coarsest velocity field: it aggregates more valid pixels, reducing noise sensitivity, but may smooth out important flow structures, especially in zones with strong velocity gradients (Ljubičić et al., 2024).

2.6. *Integrated evaluation of graphical enhancement filters and software parameterization*

An integrated analysis was conducted to comprehensively assess the impact of graphical enhancement and software parameterization on the performance of both LSPIV and optical flow methods. For each case study (Fig. 1 and Table 1), one raw video sequence was pre-processed using eight different graphical filters, described in the previous Section. Seven of these had tunable parameters, each tested across five distinct configurations (Table 2), yielding 35 pre-processed sequences; GRAY was applied once, for a total of 36 pre-processed sequences per case. Considering six raw video sequences, this approach resulted in 216 pre-processed sequences. Each of these was analyzed using two LSPIV software tools, PIVlab and SSIMS-Flow, with three processing configurations per tool (Table 3), producing 648 surface velocity estimations per software, leading to 1296 velocimetry analyses. This extensive framework enabled a detailed evaluation of how filter-parameter combinations influence the accuracy of surface velocity estimations.

To quantitatively assess the performance of optical-based surface velocity estimation under these different configurations, image-derived surface velocity estimates were compared against benchmark surface velocity profiles derived from ADCP measurements, following the methodology detailed in Alongi et al. (2023). Since ADCP cannot directly measure velocities at the free surface, surface velocities were inferred from the vertical velocity distributions using a site-specific power-law fit applied to normalized velocity-depth data (Alongi et al., 2023). The resulting reconstructed surface velocity profiles were then used as reference for validation.

To evaluate the agreement between optical estimates and ADCP-derived reference velocities, four complementary performance metrics were computed along a predefined transect: (i) the Mean Absolute Percentage Error (MAPE), Eq. (2), (ii) the Mean Percentage Error (MPE), Eq. (3), (iii) the Root Mean Square Error (RMSE), Eq. (4), and (iv) the Willmott Index (δ), Eq. (5).

$$MAPE = \frac{1}{n}\sum_{i=1}^{n}\left|\frac{V_{opt,i} - V_{ref,i}}{V_{ref,i}}\right|[\%] \tag{2}$$

$$MPE = \frac{1}{n}\sum_{i=1}^{n}\left(\frac{V_{opt,i} - V_{ref,i}}{V_{ref,i}}\right)[\%] \tag{3}$$

$$RMSE = \sqrt{\sum_{i=1}^{n}\frac{\left(V_{opt,i} - V_{ref,i}\right)^2}{n}}[m/s] \tag{4}$$

$$\delta = 1 - \frac{\sum_{i=1}^{n}\left(V_{opt,i} - V_{ref,i}\right)^2}{\sum_{i=1}^{n}\left(\left|V_{opt,i} - \overline{V_{ref}}\right| + \left|V_{ref,i} - \overline{V_{ref}}\right|\right)^2}[-] \tag{5}$$

where n refers to the total number of measurement points along the transect, $V_{opt,i}$ and $V_{ref,i}$ represent the surface velocity estimated by optical analysis and the reference surface velocity at point i, respectively, and $\overline{V_{ref}}$ is the average surface velocity value of the benchmark velocity profile. MAPE expresses the average relative deviation between estimated and reference velocities in percentage terms. MPE represents the average signed relative error and provides information on the overall bias of the estimates (over- or under-estimation of surface velocities). RMSE quantifies the average magnitude of absolute errors. The dimensionless Willmott Index (Willmott et al., 2012) ranges from 0 to 1, where 1 indicates perfect agreement and 0 indicates no agreement.

3. Results

Results are presented according to the integrated evaluation framework described in Section 2.6, considering all combinations of graphical enhancement filters and processing configurations applied to the OR and PL case studies. Detailed MAPE heatmaps are shown for representative cases (OR01 and PL01), while boxplots summarize the distribution performance metrics across all experiments.

Fig. 3 presents the MAPE values for all combinations of graphical enhancement filters and processing parameter configurations for the OR01 case study. The upper heatmap shows the results from PIVlab, while the lower panel refers to SSIMS-Flow. Columns represent the different graphical filters with five parameter settings (a-e, see Table 2), and rows correspond to the three processing configurations for each software (Ω_1^P, Ω_2^P, Ω_3^P for PIVlab; Ω_1^S, Ω_2^S, Ω_3^S for SSIMS-Flow; see Table 3). The color scale indicates MAPE values.

In the OR01 measurement, the lowest overall MAPE was 16.3%, achieved by SSIMS-Flow using the EDGE1$^{(a)}$ filter with the Ω_3^S configuration. This configuration also yielded an RMSE of 0.033 m/s and a high δ of 0.839, indicating not only low relative error but also strong agreement with the variability of the ADCP-derived reference profile. In terms of MPE, the same configuration shows a value close to zero (1.5%), indicating a negligible overall bias and confirming the robustness of this optimal setup in reproducing the reference velocities. For PIVlab, the best result was 29.6%, obtained with the EDGE2$^{(c)}$ filter and the Ω_2^P setup, corresponding to an RMSE of 0.055 m/s and δ equal to 0.622. The associated MPE for this configuration is negative (−23.6%), indicating a systematic underestimation of surface velocities. Although the relative error was higher than that of SSIMS-Flow under optimal conditions, the associated RMSE confirms a moderate absolute deviation, while the Willmott Index reflects a reasonable, though weaker, reproduction of the reference velocity profile. Conversely, the worst-performing configurations showed consistently large discrepancies across all metrics. PIVlab reached 197.3% MAPE with CAP$^{(d)}$ under Ω_2^P, corresponding to an RMSE of 0.313 m/s and $\delta = 0.136$. This configuration is associated with an extremely high positive MPE (194.5%), clearly indicating severe systematic overestimation. Similarly, SSIMS-Flow recorded 186.5% with EDGE2$^{(a)}$ under Ω_3^S, associated with an RMSE of 0.301 m/s and $\delta = 0.161$, and an equally large positive MPE (186.5%), again reflecting strong overestimation. The high RMSE values confirm substantial absolute deviations in velocity magnitude, while the very low δ indicate a poor ability to reproduce the variability of the reference profile. Although SSIMS-Flow achieved the lowest individual error under optimal conditions, it generally exhibited higher MAPE values across most configurations, with only a limited number of filter-parameter combinations producing errors comparable to the best-performing configurations. The consistency observed among MAPE, RMSE, and δ suggests that when SSIMS-Flow performs well, it achieves both low relative and absolute errors and high agreement with the reference. This is further supported by MPE values close to zero under optimal conditions, indicating minimal bias. However, outside optimal configurations, all metrics deteriorate rapidly, indicating strong sensitivity to parameterization and graphical enhancement. This behavior supports the interpretation that, despite its intensity-gradient method outperforming cross-correlation in optimal conditions, SSIMS-Flow is less robust and more sensitive to parameter and filter choices, often struggling to reliably track tracer motion. A clear pattern emerges for SSIMS-Flow: poor-performing filters consistently lead to high errors, whereas filters like EDGE1$^{(a)}$ maintain good performance across all parameter sets (MAPE values of 29.3% for Ω_1^S, 18.7% for Ω_2^S and 16.3% for Ω_3^S). PIVlab accuracy is more affected by the processing setup, notably declining under Ω_3^P, where IAs become too small in relation to tracer size, limiting displacement detection. Configurations Ω_1^P and Ω_2^P provide more consistent results, averaging around 30% MAPE for most filters. However, the CAP filter combined with Ω_2^P produces high errors in several cases, suggesting a poor synergy between this filter and the parameter set.

To provide a spatially explicit representation of the results, Fig. 4 shows the surface velocity fields obtained for the best-performing filter-parameter combinations for both PIVlab and SSIMS-Flow in the OR01 case. The figure also reports the comparison between image-derived surface velocity profiles extracted along the ADCP transect and the

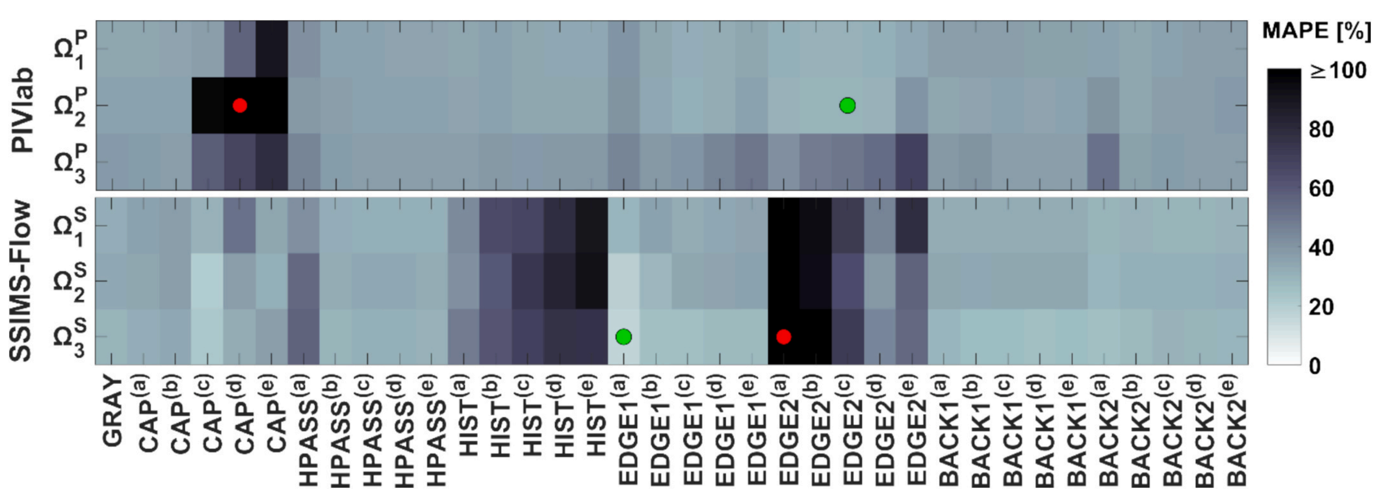

Fig. 3. Heatmaps of MAPE values for all combinations of graphical enhancement filters and processing parameter sets for the OR01 case study. The upper panel shows results from PIVlab, the lower from SSIMS-Flow. The color scale represents the MAPE: darker shades indicate errors ≥100%, lighter shades indicate errors approaching 0%. Red dots mark the worst-performing configurations (highest MAPE for each software), while green dots highlight the best-performing ones (lowest MAPE). (For interpretation of the references to colour in this figure legend, the reader is referred to the web version of this article.)

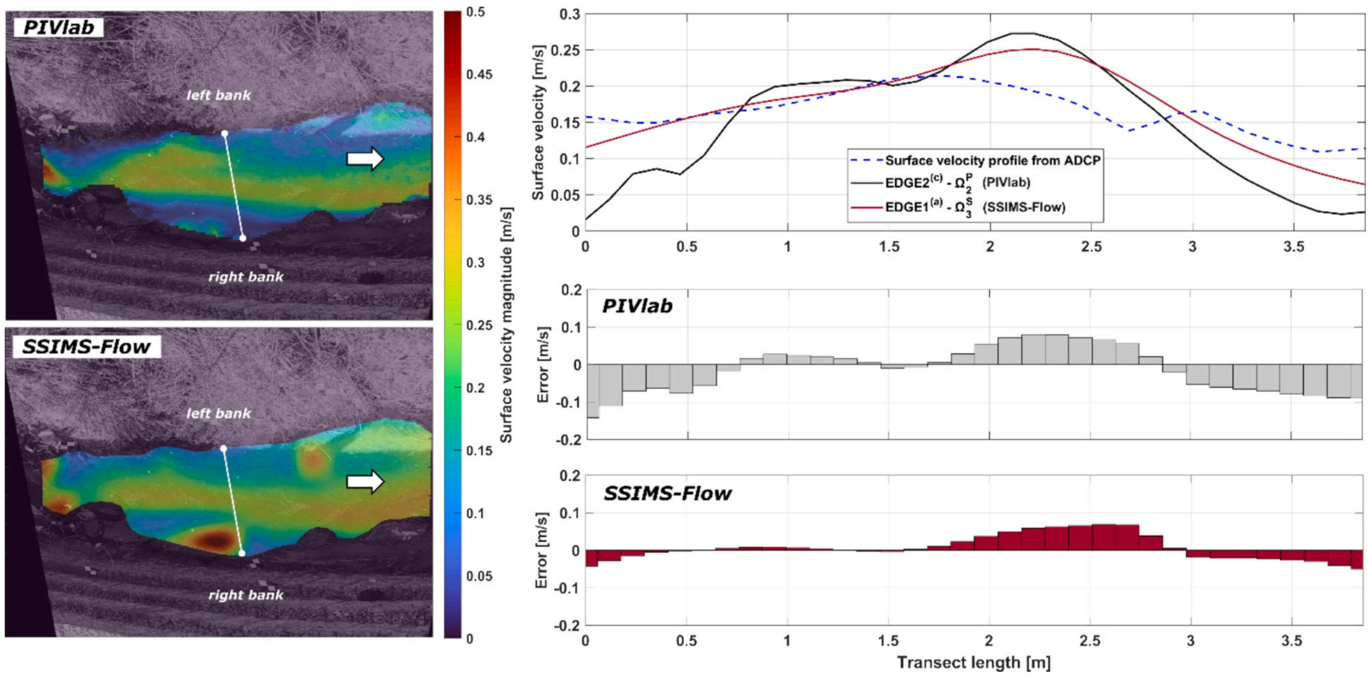

Fig. 4. Surface velocity field comparison for the OR01 case using the optimal processing configurations of PIVlab (EDGE2[(e)] $-\ \Omega_2^P$) and SSIMS-Flow (EDGE1[(a)] $-\ \Omega_3^S$). Left panels: spatial distribution of surface velocity magnitude over the recorded image domain for PIVlab (top) and SSIMS-Flow (bottom). The white line indicates the ADCP transect used for validation, while the white arrow shows the flow direction. Top-right panel: comparison between the ADCP-derived surface velocity profile (blue dashed line) and the profiles extracted from the image-derived velocity fields along the same transect (black line for PIVlab; red line for SSIMS-Flow). Middle-right and bottom-right panels: corresponding pointwise error distributions (optical technique minus ADCP reference) along the transect for PIVlab and SSIMS-Flow, respectively. (For interpretation of the references to colour in this figure legend, the reader is referred to the web version of this article.)

benchmark surface velocity profile derived from ADCP measurements.

The spatial velocity maps reported in Fig. 4 highlight a coherent main flow core located near the central portion of the channel for both software tools. PIVlab produces a relatively smooth velocity field with a gradual lateral velocity gradient, whereas SSIMS-Flow shows slightly more localized high-velocity patches, particularly in the central-right portion of the wetted section. Along the ADCP transect, both optical techniques reproduce the general shape of the surface velocity profile, including the location of the maximum velocity region. However, PIVlab tends to slightly overestimate velocities in the central portion of the transect (+0.08 m/s) and underestimate them near the right bank (−0.12 m/s). SSIMS-Flow shows a closer agreement in the upstream half of the transect but exhibits localized overestimation around the velocity peak (+0.07 m/s). The error distributions confirm these tendencies. For PIVlab, errors are moderately distributed along the transect with a tendency towards positive deviations in the central region. SSIMS-Flow presents a more concentrated positive error peak near the maximum velocity zone, while maintaining smaller deviations in the lateral portions.

Fig. 5 summarizes the MAPE, MPE, RMSE and δ values for all three OR measurements via boxplots, showing the distribution of errors across the tested filter-parameter configurations.

The boxplots for OR01 confirm the results shown in Fig. 3, highlighting the more stable performance of PIVlab. This behavior is consistently reflected by the corresponding MPE, RMSE, and δ distributions, which show limited dispersion and comparatively higher levels of agreement across parameter sets. Similarly, in OR02 and OR03, PIVlab consistently outperformed SSIMS-Flow, yielding lower and more stable MAPE values. In OR02, PIVlab reported average MAPE ranging from 28.6% to 67.8%, with the best result for the Ω_3^P configuration ($MAPE_{avg}$ = 28.6% and IQR = 11.8%), while SSIMS-Flow showed extremely high MAPE values, all exceeding 240%, indicating poor agreement with the ADCP reference. This degradation is further evidenced by the corresponding increase in average RMSE and the marked reduction in the average Willmott Index. PIVlab registered average RMSE values ranging between 0.026 and 0.056 m/s, whereas SSIMS-Flow was characterized by substantially higher average RMSE values (0.191–0.204 m/s). The robustness of PIVlab across processing setups and graphical enhancement filters is further confirmed by the δ_{avg}, which consistently remained above 0.700 (0.848 for Ω_1^P, 0.707 for Ω_2^P, and 0.886 for Ω_3^P). In contrast, SSIMS-Flow exhibited markedly lower agreement levels, with δ_{avg} values of 0.219, 0.208, and 0.219 for Ω_1^S, Ω_2^S, and Ω_3^S, respectively. The MPE boxplots provide additional insight into the nature of these discrepancies. In OR02, PIVlab, maintains predominantly low MPE_{avg} values (17.9% for Ω_1^P, 51.1% for Ω_2^P, −4.4% for Ω_3^P) with relatively narrow interquartile ranges (37.3%, 34%, 32.5%, respectively), confirming a limited variability across configurations. Conversely, SSIMS-Flow shows strongly positive MPE_{avg} values (238.5% for Ω_1^S, 248.6% for Ω_2^S, 238.5% for Ω_3^S), with very large dispersion (>56.6%). This indicates a pronounced and unstable overestimation behavior, which aligns with the extremely high MAPE and RMSE values observed for the same dataset. Similar results were found for OR03, where PIVlab achieved average MAPE between 55.2% and 71.2%, compared to 173.8% to 178.5% for SSIMS-Flow. similarly, the average RMSE for SSIMS-Flow also reflects poorer performance compared to PIVlab ($RMSE_{avg}$ between 0.070 and 0.079 m/s for PIVlab, between 0.160 and 0.176 m/s for SSIMS-Flow). Although the discrepancy in average RMSE is moderate, the maximum RMSE observed with PIVlab does not exceed 0.202 m/s, whereas for SSIMS-Flow, maximum RMSE values range between 0.379 and 0.408 m/s. A similar patterns is observed for the Willmott Index, which shows average values between 0.642 and 0.713 for PIVlab, compared to 0.474 – 0.517 for SSIMS-Flow. The MPE distributions in OR03 reinforce these findings. PIVlab retains a predominantly negative (−16.5% for Ω_1^P, 1.5% for Ω_2^P, −27.6% for Ω_3^P) and relatively compact MPE distribution, confirming a systematic but stable underestimation of surface velocities. In contrast, SSIMS-Flow exhibits consistently positive MPE values (147.8% for Ω_1^S, 156% for

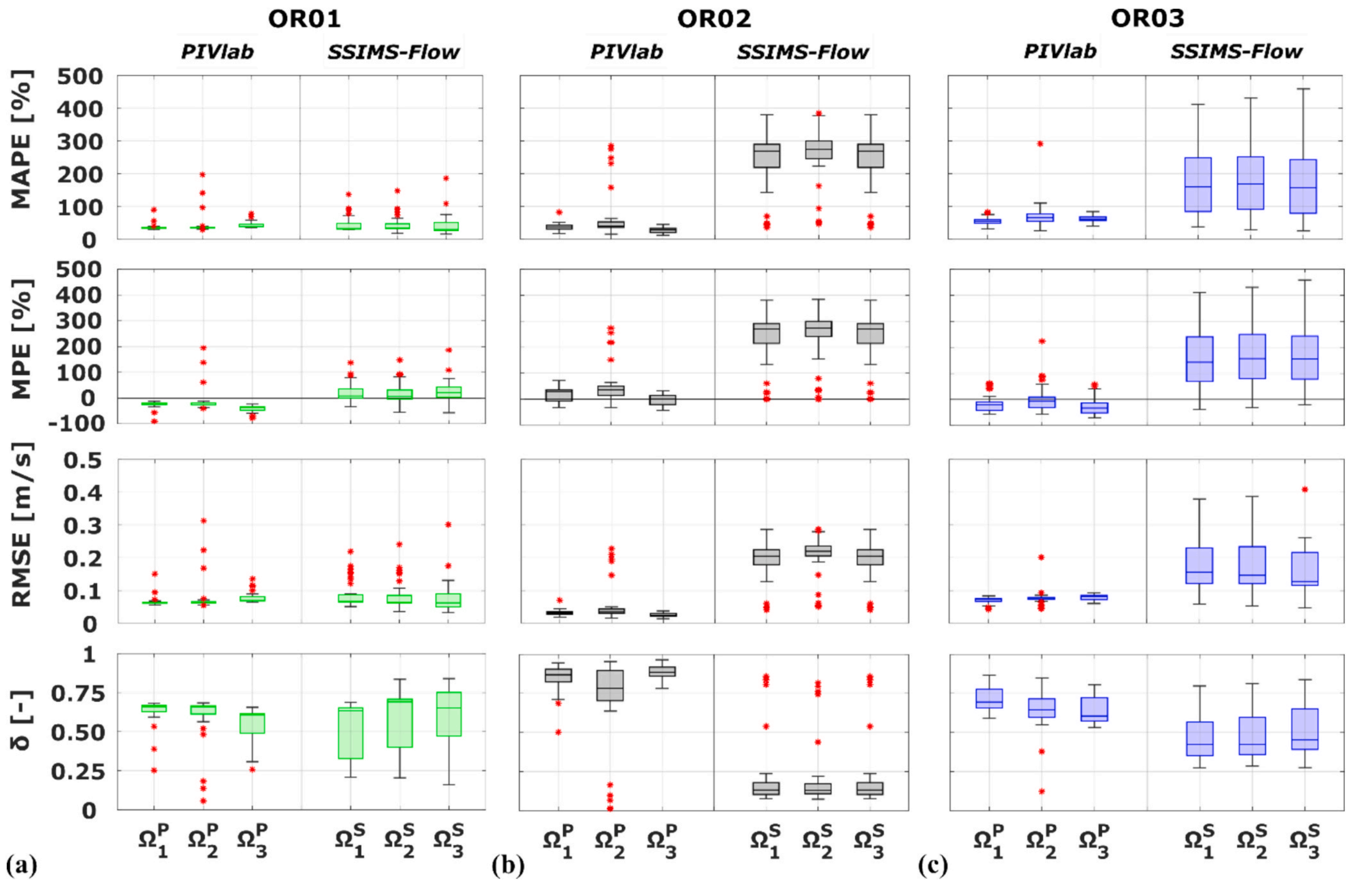

Fig. 5. Boxplots of performance metrics for the (a) OR01, (b) OR02, and (c) OR03 case studies. Rows display MAPE, MPE, RMSE, and Willmott Index δ. In each panel, six boxplots illustrating the distribution of metric values obtained using PIVlab and SSIMS-Flow under three different processing parameter sets (Ω_1^P, Ω_2^P, Ω_3^P, and Ω_1^S, Ω_2^S, Ω_3^S). For each configuration, boxplots summarize the results obtained by applying all tested graphical enhancement filters and their respective configurations (a–e). The first three boxplots in each panel refer to PIVlab, while the remaining three correspond to SSIMS-Flow.

Ω_2^S, 158.2% for Ω_3^S) with wide interquartile ranges and numerous extreme outliers, indicating strong and highly variable overestimation. Although PIVlab errors were higher in OR03 than in OR02, the performance metrics IQRs remained relatively narrow, reflecting consistent performance across filter and parameter combinations. Conversely, SSIMS-Flow exhibited wide IQRs, revealing high sensitivity to input variations and unstable outputs. PIVlab minimum MAPE reached 26.1% (BACK2$^{(e)}$ under Ω_2^P), but in the CAP$^{(d)}$- Ω_2^P configuration MAPE peaked at 292.3%, while SSIMS-Flow maximum errors reached 458.9% (EDGE2$^{(a)}$ under Ω_3^S), with a lowest minimum of 25.6% (EDGE1$^{(e)}$ under Ω_3^S). These extreme cases are also associated with very large positive MPE values for SSIMS-Flow, confirming that such failures correspond to severe overestimation rather than random error. In terms of RMSE, the largest error recorded was 0.408 m/s, corresponding to the configuration where the maximum MAPE (548.9%) was observed (EDGE2$^{(a)}$ under Ω_3^S), with a related δ of 0.276. Conversely, PIVlab performed best with a minimum RMSE of 0.043 m/s in its optimal configuration, associated with a δ approaching 0.900. Overall, OR03 yielded higher errors, particularly for SSIMS-Flow. The occurrence of such massive errors (e.g., MAPE exceeding 400%) should not be interpreted as a marginal inaccuracy of the methodology, but rather as a total algorithmic failure triggered by specific filter-parameter combinations. In these cases, the graphical enhancement likely degraded the tracer signal-to-noise ratio to a point where the software was unable to distinguish physical motion from background artifacts.

These differences likely arise from the visible riverbed in the sequences (as highlighted by NDTI characterizing the acquired sequences: OR01 = −0.146; OR02 = 0.005; OR03 = 0.058), which introduces visual noise. The PIVlab cross-correlation approach was relatively robust, averaging out background inconsistencies by focusing on coherent displacement patterns. In contrast, SSIMS-Flow relies on intensity gradient analysis, which is more sensitive to visual artifacts. Background textures and reflections may create false gradients misinterpreted as tracer movements, degrading velocity estimates and causing the observed instability and large errors.

A markedly different scenario is observed in the PL case study (Fig. 6). All PL measurements feature a uniform, non-transparent background, with NDTI values above 0.100 (turbid water), unlike the OR cases, where NDTI values near zero indicated of high water clarity. The absence of background textures or visible riverbed eliminates visual noise, inherently enhancing tracer contrast and potentially improving the accuracy of surface velocity estimations.

In contrast to the OR01 case (Fig. 3), the performance gap between the two software tools is significantly reduced. While PIVlab still shows slightly lower overall errors, with $MAPE_{avg}$ values of 38.8%, 46.9%, and 38.6% for setups Ω_1^P, Ω_2^P, Ω_3^P, SSIMS-Flow exhibits a notable improvement, reporting average errors of 36.1%, 35.8%, and 33.2% (setups Ω_1^S, Ω_2^S, Ω_3^S, respectively). In terms of RMSE, the average errors obtained by both software tools are very similar, with $RMSE_{avg}$ ranging between 0.090 and 0.120 m/s. A comparable pattern is observed when considering the average Willmott Index, for which both tools show moderate performance, with values not exceeding 0.445 and not dropping below 0.417. However, the MPE analysis reveals a key difference in the behavior of the two approaches. Both PIVlab and SSIMS-Flow are characterized by predominantly negative MPE values across almost all filter and parameter combinations, indicating a systematic

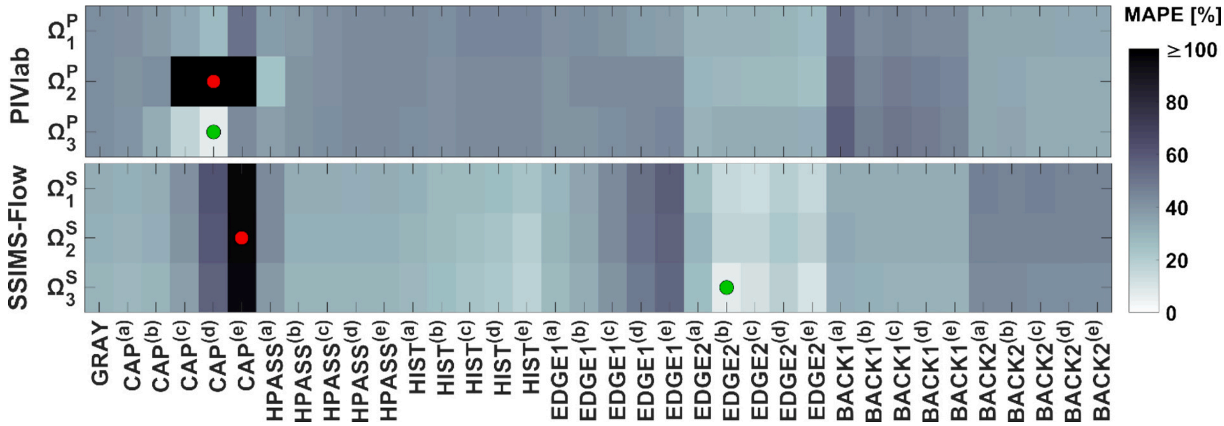

Fig. 6. Heatmaps of MAPE values for all combinations of graphical enhancement filters and processing parameter sets, referring to the PL01 case study.

underestimation of surface velocities. For PIVlab, MPE values are generally concentrated between approximately −25% and −45%, with relatively limited variability across configurations, suggesting a stable and consistent negative bias. SSIMS-Flow also shows negative MPE values in most cases, typically ranging between −20% and −60%, and reaching even more pronounced underestimation for specific filters such as CAP$^{(e)}$, where MPE approaches −100%. These results are not only much lower than those obtained in OR02 and OR03, but in some cases even outperform PIVlab, particularly under the Ω_3^S configuration. This suggests that the uniform background, as indicated by high NDTI values, mitigates the sensitivity of the SSIMS-Flow algorithm to false positives caused by background textures in the OR cases. Furthermore, both software packages show more consistent responses across filters and settings: poorly performing configurations in one tend to yield similar results in the other. For example, CAP$^{(e)}$ leads to the worst errors for both tools, confirming its instability regardless of context. Conversely, configurations such as EDGE2$^{(b)}$, BACK2$^{(b)}$, and some HIST variants consistently produce lower MAPE values. Overall, in uniform, low-noise scenarios, the choice of graphical enhancement becomes more influential than the choice of the software, underscoring the central role of filter selection in ensuring accurate image-based measurements.

Fig. 7 reports the results obtained for the PL01 case, showing the surface velocity fields derived from the optimal configurations of PIVlab and SSIMS-Flow and their comparison with the ADCP-based reference along the measurement transect.

In PL01, the velocity field reconstructed by both software tools displays the highest magnitudes concentrated in the central flow corridor and progressively decreasing toward both banks. Neither method exhibits spurious high-velocity spots or unrealistic discontinuities in the flow field, which supports the robustness of the optimal filter-parameter combinations selected. The extracted velocity profiles show a very close agreement with the ADCP-derived reference along most of the transect. The position and magnitude of the velocity maximum are well captured by both techniques, and discrepancies remain limited across the entire cross-section. In terms of error, deviations are generally small ($< \pm 0.05$ m/s) and spatially smooth. PIVlab exhibits predominantly negative

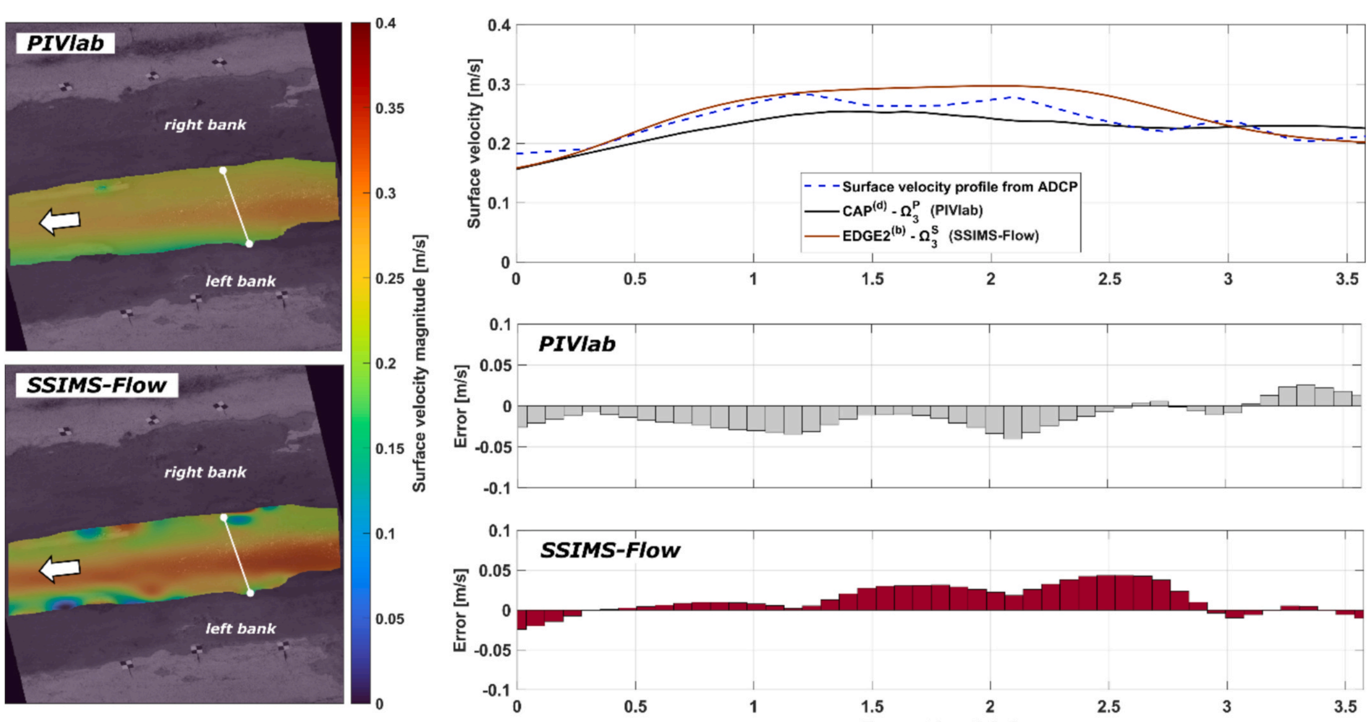

Fig. 7. Surface velocity field comparison for the PL01 case using the optimal processing configurations of PIVlab (CAP$^{(d)}$ − Ω_3^P) and SSIMS-Flow (EDGE2$^{(b)}$ − Ω_3^S).

errors along the central portion of the transect, within approximately −0.03 to −0.05 m/s, indicating a slight underestimation of the velocity peak. SSIMS-Flow shows modest positive deviations in the mid-section, generally not exceeding + 0.05 m/s, with near-zero errors toward the banks.

Results for the PL02 and PL03 scenarios are summarized alongside PL01 using boxplots, which illustrate the variability of MAPE, RMSE, and δ values across all tested filter and parameter combinations. This provides a comprehensive overview of the performance and robustness of both PIVlab and SSIMS-Flow under the uniform background conditions characteristic of the PL measurements (Fig. 8).

The results in Fig. 8 continue to reflect the influence of the visual conditions, such as uniformity and the absence of noise or textures in the background, as already noted in PL01. In PL02, both software tools exhibit improved performance compared to the OR cases. PIVlab reports mean MAPE values between 31.7% (Ω_1^P, Ω_2^P) and 36.9% (Ω_3^P), with errors ranging from 7.8% to 58.2%. However, the relatively wide IQRs (up to 32.4% in Ω_3^P) indicate some sensitivity to filter-parameter combinations. SSIMS-Flow performs slightly better overall, with mean MAPE values from 14.4% to 18.3%, and a tighter spread of results (IQR down to 3.3% in Ω_3^S), suggesting more stable behaviour under uniform visual conditions. In this case, the Willmott Index reaches its highest value for SSIMS-Flow, with δ_{avg} values of 0.923, 0.928, and 0.863 for Ω_1^S, Ω_2^S, and Ω_3^S, respectively. PIVlab also returns relatively high Willmott Index values, averaging 0.700 for Ω_1^P and Ω_2^P, and 0.559 for Ω_3^P. Consistently, average RMSE values remain low for both tools, ranging between 0.031 and 0.034 m/s for SSIMS-Flow and between 0.066 and 0.079 m/s for PIVlab. In PL03, differences between the tools remain observable. PIVlab achieves $MAPE_{avg}$ from 21.8% to 36.2%, with minimum and maximum errors of 8% and 81.2%, respectively. The IQRs, though moderate (23.5–30.4%), reflect some variability across configurations. SSIMS-Flow, by contrast, provides comparable average accuracy ($MAPE_{avg}$ from 31.3% to 38.1%) but shows more stable results, with narrower IQRs (e.g., 11.3% in Ω_3^S) despite a higher maximum error (97.7%). PIVlab shows slightly negative average bias, with MPE_{avg} values of −24.2%, −2.4%, and −24.6% for Ω_1^P, Ω_2^P, and Ω_3^P, respectively, but is characterized by relatively high variability, as evidenced by IQR values reaching 22.2%. this indicates that, although the average bias is moderate, the method is sensitive to specific filter-parameter combinations, which can produce both underestimation and occasion overestimation. In contrast, SSIMS-Flow, exhibits MPE_{avg} close to zero (1.5%, 1.6%, and 5.1% for Ω_1^S, Ω_2^S, and Ω_3^S, respectively), together with lower variability (IQR values below 7%). This indicates a substantially reduced and more stable bias.

4. Discussion

The comparative analysis carried out in this work highlights how both environmental conditions and methodological choices critically influence the accuracy of optical-based surface velocity estimations. The NDTI, used here as a qualitative indicator of water clarity, supports an objective distinction between the case studies: the OR sequences, with NDTI values close to zero or negative, were characterized by transparent water and visible riverbeds, while PL sequences, with NDTI values above 0.10, presented uniform and turbid backgrounds.

Under the more complex visual conditions of the OR measurements, PIVlab proved more robust and stable, consistently yielding lower MAPE values. This can be attributed to the nature of its cross-correlation algorithm, which is less sensitive to background textures and more effective in detecting dominant displacement patterns, especially when appropriate IAs are used. On the contrary, SSIMS-Flow showed higher sensitivity to both filter choice and environmental complexity, often resulting in large errors due to its reliance on pixel-wise intensity gradients, which are more easily disturbed by background noise. However, in the PL cases, characterized by more homogeneous water surfaces (as

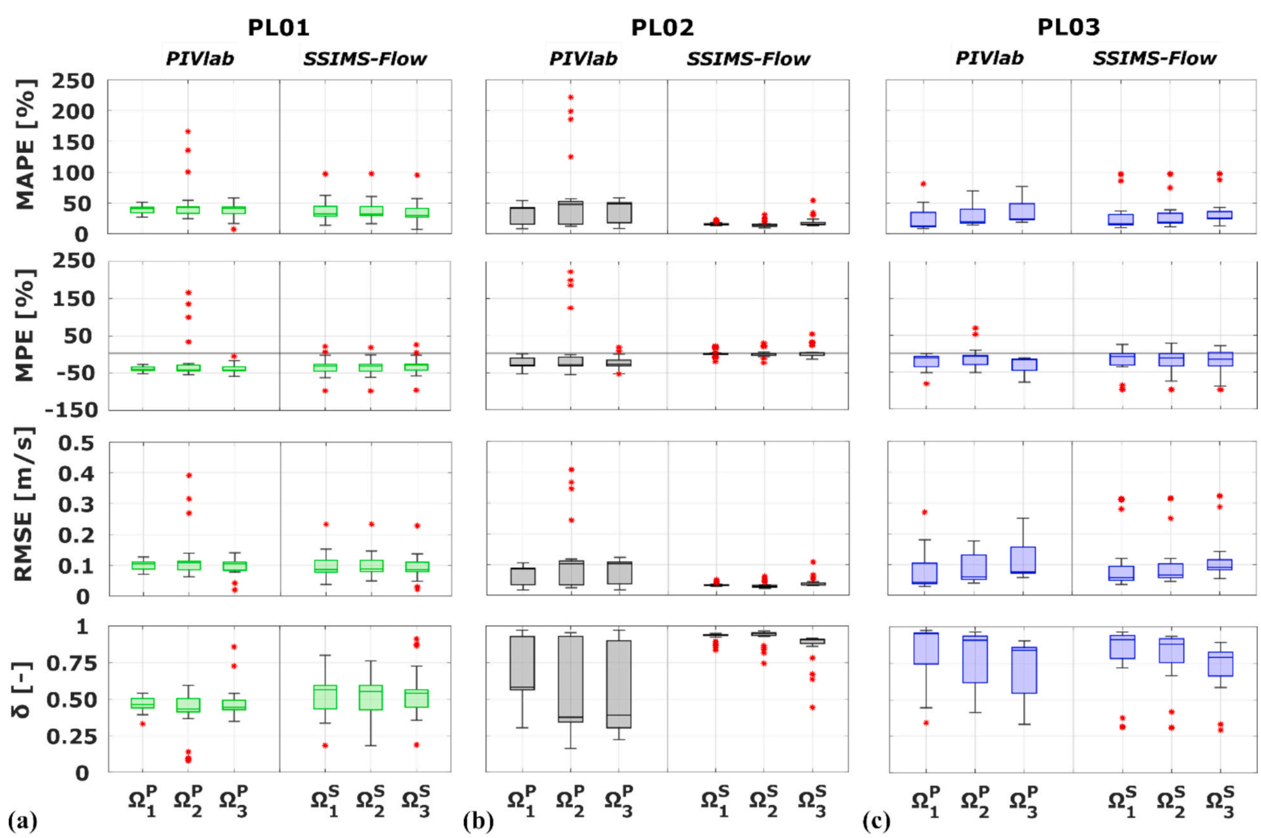

Fig. 8. Boxplots of MAPE, MPE, RMSE, and Willmott Index δ values for the (a) PL01, (b) PL02, and (c) PL03 case studies.

indicated by NDTI), SSIMS-Flow performance improved significantly, occasionally outperforming PIVlab. This suggests that, under favourable visual conditions and with appropriate pre-processing, optical flow-based methods can achieve comparable or even higher accuracy.

The contrasting results between the OR and PL sequences underscore the pivotal role of background uniformity and image quality. In the OR cases, low NDTI values ($\leq$0.058) confirmed high water transparency, with visible riverbeds and sunlight reflections introducing complex background textures. These features particularly affected SSIMS-Flow, which relies on intensity gradients and is inherently prone to interpret any pixel variation as motion, thus making it more sensitive to visual noise unless additional filters or modifications are applied. In contrast, the PL sequences, with higher NDTI values ($>$0.100), featured turbid water and a uniform concrete bed, enhancing tracer visibility and reducing background interference. This setting proved favourable for both software tools, enabling more accurate velocity estimations.

The choice of graphical enhancement filters proved critical for LSPIV accuracy. Filters like EDGE1 (Sobel filter) and BACK2 (RGB-based background subtraction) consistently yielded lower MAPE values, as they effectively enhanced tracer definition and suppressed background noise, regardless of water clarity or lighting. On the other hand, CAP frequently resulted in high errors, likely due to its tendency to distort tracer features by amplifying intensity extremes.

The variability in performance across filters also highlights that a one-size-fits-all approach is ineffective: the choice of the filter should be tailored to the specific visual characteristics of each video, including lighting, background uniformity, and tracer colour. This implies that image-based velocimetry cannot rely on fixed or default parameter settings, which end users should approach with caution as they often fail to account for site-specific environmental variability. Consequently, a preliminary "trial-and-error" phase remains a necessary step to ensure the reliability of the velocity estimates.

Software parameterization also had a marked effect on LSPIV outcomes. In PIVlab, very small IAs reduced accuracy, likely due to insufficient tracer content in noisy or low-seeding conditions. However, a more critical factor is that if the IA is very small, tracers might move out of the IA during the time period between frames, in which case they might as well never have been there at all, leading to loss of correlation, particle escape, and unreliable or missing vectors (Legleiter and Kinzel, 2024a). Conversely, while larger IAs improved robustness by ensuring tracer persistence within the window, they reduced spatial detail and limited the ability to detect the very low velocities characteristic of the study areas. SSIMS-Flow showed a similar trade-off: small pooling blocks preserved detail but increased sensitivity to noise while larger blocks enhanced stability at the cost of resolution. Intermediate configurations generally balanced accuracy and robustness, particularly in sequences with uniform visual conditions.

To generalize the findings, a frequency analysis was performed to identify which filters are more likely to produce the best or the worst results in terms of MAPE across all case studies and configurations. For each software and processing setup, the analysis recorded how frequently a given filter resulted in the lowest ("best") or highest ("worst") error. The results, summarized in Table 4, show the percentage of occurrences in which each filter ranked as the best or the worst performer for both PIVlab and SSIMS-Flow. This synthesis provides a broader view of each filter's robustness and general reliability, beyond single-case observations.

The CAP filter is consistently the worst performer for PIVlab, ranking as the "worst" in 61% of configurations. As for SSIMS-Flow, the poorest performance is usually associated with EDGE2 (44%). Other filters, such as HPASS, EDGE1, and BACK1, are occasionally identified as poor performers, though with much lower frequencies. Conversely, EDGE2 emerges as the most frequent "best" performer for PIVlab (28%), while for SSIMS-Flow, both EDGE1 and EDGE2 top the ranking in 33% of cases. Notably, despite its overall instability, the CAP filter also appears among the best performers in 22% of cases for both tools, highlighting its highly context-dependent behaviour.

An interesting outcome of the analysis is the neutral performance of the GRAY filter, which was never classified as either best or worst. This suggests that, while GRAY offers a stable baseline due to its simplicity, its lack of targeted enhancement limits its effectiveness in complex visual scenarios. Another key insight is the higher performance of non-traditional filters, which more frequently yielded the lowest MAPE values. These filters appear better suited to the needs of image velocimetry, enhancing tracer definition more effectively than traditional options. In contrast, traditional filters, particularly CAP and HPASS, were often associated with poor outcomes, likely due to their tendency to distort tracer features. This highlights the need for careful selection of enhancement techniques, as conventional methods may not align with the demands of modern LSPIV analysis.

The analysis further demonstrated that software parameterization heavily influences outcomes. In PIVlab, performance drops when interrogation areas become too small, which can occur because tracer may move across too many pixels between consecutive frames, leading to insufficient correlation within the interrogation window. This effect is especially pronounced when small interrogation areas are combined with unsuitable filters (e.g., CAP), further reducing measurement accuracy. SSIMS-Flow performance is more sensitive to filter choice and background conditions but greatly benefits from uniform backgrounds and edge-enhancing filters.

The findings of this study have practical implications for practitioners employing LSPIV techniques in the field. Firstly, the selection of graphical filters and parameter settings should not be overlooked, as they significantly influence the accuracy of the estimated velocity field. Secondly, while traditional cross-correlation software like PIVlab offers higher resilience to suboptimal visual conditions such as those with clear water and visible riverbed, newer gradient-based tools like SSIMS-Flow can outperform when paired with careful pre-processing and in favourable visual environments. Therefore, the optimal software selection should account for both algorithm type and site-specific image quality. Moreover, results underline the need for adaptive workflows, where filter and parameter configurations are tested on sample frames before full analysis.

Table 4
Frequency (%) with which each enhancement filter was classified as the best (top table) and the worst (bottom table) performer based on MAPE values, across all tested configurations for PIVlab and SSIMS-Flow. The highest frequencies for each software are highlighted in bold.

	GRAY	CAP	HPASS	HIST	EDGE1	EDGE2	BACK1	BACK2
				Best performer				
PIVlab	0%	22%	6%	0%	22%	**28%**	0%	22%
SSIMS-Flow	0%	22%	11%	0%	**33%**	**33%**	0%	0%
				Worst performer				
PIVlab	0%	**61%**	6%	0%	11%	6%	17%	0%
SSIMS-Flow	0%	22%	0%	17%	0%	**44%**	0%	17%

5. Conclusions

This study presented an in-depth sensitivity analysis of image-based surface velocity estimation techniques, focusing on the combined effects of graphical enhancement filters and software parameterization. By analysing over 1200 configurations from two field case studies, this work offers a comprehensive assessment of how pre-processing and software settings jointly impact image-based measurements. Unlike existing works that treated these aspects separately, the integrated approach adopted here provides novel insights into their combined effects. The comparative evaluation of PIVlab and SSIMS-Flow revealed that cross-correlation methods (PIVlab) are generally more robust under challenging visual conditions, whereas intensity-gradient methods (SSIMS-Flow) can deliver higher accuracy and spatial detail under visually uniform and well-defined surface conditions. Notably, the Normalized Difference Turbidity Index (NDTI) proved to be a valuable objective metric for pre-characterizing the monitoring site and guiding the selection of the most suitable computational approach.

Beyond methodological insights, the study provides practical guidance for LSPIV and optical flow users, emphasizing the importance of adaptive, case-specific workflows over default or fixed settings. Key findings include:

- Graphical enhancement filters are critical. Non-traditional filters, particularly edge detectors and RGB-based background subtraction methods, consistently outperformed the standard ones, e.g., contrast capping and high-pass filters.
- Filter-parameter interactions matter. Performance depends not only on the filter or parameter alone, but on their combination, reinforcing the need for integrated testing.
- PIVlab is more robust in noisy or low-contrast conditions, while SSIMS-Flow excels in visually homogeneous environments.
- Traditional filters (e.g., GRAY, CAP, HPASS) were rarely among the best-performing configurations and, in some cases, degraded tracer clarity.
- Optimal parameterization depends on tracer visibility and background complexity which can be measured by NDTI. Larger IAs (PIVlab) or pooling blocks (SSIMS-Flow) may improve stability in noisy images but may oversmooth fine-scale motion; intermediate settings generally offered the best trade-off.

While the results provide meaningful methodological guidance, limitations must be acknowledged. The dataset consists of six sequences from two Sicilian rivers with relatively small widths and low velocities (< 0.5 m/s). These conditions enabled controlled sensitivity testing under low-energy hydraulic regimes but do not represent the full range of river environments. In larger and more energetic systems, increased turbulence and larger-scale surface features could influence the behaviour of both cross-correlation and optical flow algorithms. Thus, the findings should be regarded as representative of small-to-medium systems and might require adaptation before being applied to larger rivers. The study also relied on artificial tracers to ensure a controlled seeding density. Although necessary for methodological consistency, this choice does not fully capture the challenges associated with natural surface features, whose lower contrast and more stochastic behaviour can affect filter performance and tracking stability. Likewise, the evaluation focused on a finite set of graphical filters applied individually. More complex enhancement pipelines involving sequential combinations, i.e., "stacking", of filters may further improve tracer visibility but were not explored here due to the exponential increase in computational complexity. It should be also noted that the accuracy assessment presented in this study is based exclusively on velocity magnitude; the directional component of the velocity field was not included in the quantitative validation, and this aspect should be considered when interpreting the reported performance metrics.

Future research should therefore focus on expanding the proposed workflow to a broader range of hydraulic, geomorphic, and environmental settings, including larger rivers and open-access datasets. Applying the NDTI-based characterization and integrated filter-parameter analysis to diverse conditions will be essential for assessing the broader scalability of the framework. Advancing toward semi-adaptive or fully adaptive workflows that automatically tune filters and processing parameters based on scene characteristics represents a promising direction to reduce manual tuning and enhance the applicability of image-based velocimetry for large-scale and long-term hydrological monitoring.

CRediT authorship contribution statement

Francesco Alongi: Writing – review & editing, Writing – original draft, Visualization, Validation, Software, Methodology, Investigation, Formal analysis, Data curation, Conceptualization. **Robert Ljubičić:** Writing – review & editing, Writing – original draft, Visualization, Validation, Software, Methodology, Investigation, Formal analysis, Data curation, Conceptualization. **Silvano Fortunato Dal Sasso:** Writing – review & editing, Writing – original draft, Visualization, Validation, Supervision, Software, Project administration, Methodology, Investigation, Funding acquisition, Formal analysis, Conceptualization. **Leonardo Valerio Noto:** Writing – review & editing, Visualization, Validation, Supervision, Project administration, Methodology, Funding acquisition, Conceptualization.

Declaration of competing interest

The authors declare that they have no known competing financial interests or personal relationships that could have appeared to influence the work reported in this paper.

Acknowledgments

Field campaigns were carried out within the research agreement MONITORPORT2 entitled "*Accordo di collaborazione scientifica per l'effettuazione di una campagna triennale di misure di portata per l'elaborazione delle scale di deflusso sotto il coordinamento tecnico di ISPRA per supportare il progetto sul bilancio idrologico nazionale, in corso di realizzazione da parte di ISPRA*" (CUP: F62G16000000001), between the Regional Basin's Authority of Sicily (Autorità di Bacino del Distretto Idrografico della Sicilia) and the Department of Engineering of the University of Palermo.

The work was supported by the DIGIDRAIN project (funding from the Science Fund of the Republic of Serbia, research program DIASPORA 2023: joint research, under grant agreement number: 17823 – *City-scale digital twins for urban drainage systems: bringing "smart" to water infrastructure*).

We sincerely thank the Reviewers for their thorough and constructive revisions of the manuscript. Their comments and suggestions have significantly improved the clarity, structure, and overall quality of the paper.

Appendix A. Supplementary data

Supplementary data to this article can be found online at https://doi.org/10.1016/j.jhydrol.2026.135780.

Data availability

Data will be made available on request.

References

Abril, J.B., Knight, D.W., 2004. Stage-discharge prediction for rivers in flood applying a depth-averaged model. J. Hydraul. Res. 42, 616–629. https://doi.org/10.1080/00221686.2004.9628315.

Acharya, B.S., Bhandari, M., Bandini, F., Pizarro, A., Perks, M., Joshi, D.R., Wang, S., Dogwiler, T., Ray, R.L., Kharel, G., Sharma, S., 2021. Unmanned aerial vehicles in hydrology and water management: applications, challenges, and perspectives. Water Resour. Res. 57, e2021WR029925. https://doi.org/10.1029/2021WR029925.

Admiraal, D.M., Stansbury, J.S., Haberman, C.J., 2004. Case study: particle velocimetry in a model of lake Ogallala. J. Hydraul. Eng. 130, 599–607. https://doi.org/10.1061/(ASCE)0733-9429(2004)130:7(599).

Alongi, F., Pumo, D., Nasello, C., Nizza, S., Ciraolo, G., Noto, L.V., 2023. An automatic ANN-based procedure for detecting optimal image sequences supporting LS-PIV applications for rivers monitoring. J. Hydrol. 626, 130233. https://doi.org/10.1016/j.jhydrol.2023.130233.

Anwar Sadat, M., Guan, Y., Zhang, D., Shao, G., Cheng, X., Yang, Y., 2020. The associations between river health and water resources management lead to the assessment of river state. Ecol. Ind. 109, 105814. https://doi.org/10.1016/j.ecolind.2019.105814.

Birgand, F., Lellouche, G., Appelboom, T.W., 2013. Measuring flow in non-ideal conditions for short-term projects: uncertainties associated with the use of stage-discharge rating curves. J. Hydrol. 503, 186–195. https://doi.org/10.1016/j.jhydrol.2013.09.007.

Bodart, G., Le Coz, J., Jodeau, M., Hauet, A., 2022. Synthetic river flow videos for evaluating image-based velocimetry methods. Water Resour. Res. 58. https://doi.org/10.1029/2022WR032251.

Camarasa-Belmonte, A.M., 2021. Flash-flooding of ephemeral streams in the context of climate change. CIG 47, 121–142. https://doi.org/10.18172/cig.4838.

Chen, M., Chen, H., Wu, Z., Huang, Y., Zhou, N., Xu, C.-Y., 2024. A review on the video-based river discharge measurement technique. Sensors 24, 4655. https://doi.org/10.3390/s24144655.

Choi, K.-H., Ha, J.-E., 2021. An adaptive threshold for the canny algorithm with deep reinforcement learning. IEEE Access 9, 156846–156856. https://doi.org/10.1109/ACCESS.2021.3130132.

Creutin, J.D., Muste, M., Bradley, A.A., Kim, S.C., Kruger, A., 2003. River gauging using PIV techniques: a proof of concept experiment on the Iowa River. J. Hydrol. 277, 182–194. https://doi.org/10.1016/S0022-1694(03)00081-7.

Dabire, N., Ezin, E.C., Firmin, A.M., 2024. Water quality assessment using normalized difference index by applying remote sensing techniques: case of Lake Nokoue. In: 2024 IEEE 15th Control and System Graduate Research Colloquium (ICSGRC). Presented at the 2024 IEEE 15th Control and System Graduate Research Colloquium (ICSGRC), pp. 1–6. https://doi.org/10.1109/ICSGRC62081.2024.10690936.

Dal Sasso, S.F., Pizarro, A., Manfreda, S., 2021a. Recent advancements and perspectives in UAS-based image velocimetry. Drones 5, 81. https://doi.org/10.3390/drones5030081.

Dal Sasso, S.F., Pizarro, A., Pearce, S., Maddock, I., Manfreda, S., 2021b. Increasing LSPIV performances by exploiting the seeding distribution index at different spatial scales. J. Hydrol. 598, 126438. https://doi.org/10.1016/j.jhydrol.2021.126438.

Depetris, P.J., 2021. The importance of monitoring river water discharge. Front. Water 3, 745912. https://doi.org/10.3389/frwa.2021.745912.

Dramais, G., Le Coz, J., Camenen, B., Hauet, A., 2011. Advantages of a mobile LSPIV method for measuring flood discharges and improving stage–discharge curves. J. Hydro Environ. Res. 5, 301–312. https://doi.org/10.1016/j.jher.2010.12.005.

Ellison, J.C., Smethurst, P.J., Morrison, B.M., Keast, D., Almeida, A., Taylor, P., Bai, Q., Penton, D.J., Yu, H., 2019. Real-time river monitoring supports community management of low-flow periods. J. Hydrol. 572, 839–850. https://doi.org/10.1016/j.jhydrol.2019.03.035.

Farnebäck, G., 2003. Two-frame motion estimation based on polynomial expansion. In: Bigun, J., Gustavsson, T. (Eds.), Image Analysis, Lecture Notes in Computer Science. Springer, Berlin Heidelberg, Berlin, Heidelberg, pp. 363–370. https://doi.org/10.1007/3-540-45103-X_50.

Fujita, I., Muste, M., Kruger, A., 1998. Large-scale particle image velocimetry for flow analysis in hydraulic engineering applications. J. Hydraul. Res. 36, 397–414.

Fujita, I., Shibano, T., Tani, K., 2020. Application of masked two-dimensional Fourier spectra for improving the accuracy of STIV-based river surface flow velocity measurements. Meas. Sci. Technol. 31, 094015. https://doi.org/10.1088/1361-6501/ab808a.

Giannopoulos, A., Passaggia, P.-Y., Mazellier, N., Aider, J.-L., 2022. On the optimal window size in optical flow and cross-correlation in particle image velocimetry: application to turbulent flows. Exp. Fluids 63. https://doi.org/10.1007/s00348-022-03410-z.

Gracchi, T., Rossi, G., Tacconi Stefanelli, C., Tanteri, L., Pozzani, R., Moretti, S., 2021. Tracking the evolution of riverbed morphology on the basis of UAV photogrammetry. Remote Sens. (Basel) 13, 829. https://doi.org/10.3390/rs13040829.

Guven, A., Aytek, A., Azamathulla, H.M., 2013. A practical approach to formulate stage–discharge relationship in natural rivers. Neural Comput. & Applic. 23, 873–880. https://doi.org/10.1007/s00521-012-1011-5.

Iqbal, U., Riaz, M.Z.B., Zhao, J., Barthelemy, J., Perez, P., 2023. Drones for flood monitoring, mapping and detection: a bibliometric review. Drones 7, 32. https://doi.org/10.3390/drones7010032.

Jolley, M.J., Russell, A.J., Quinn, P.F., Perks, M.T., 2021. Considerations when applying large-scale PIV and PTV for determining river flow velocity. Front. Water 3, 709269. https://doi.org/10.3389/frwa.2021.709269.

Kantoush, S.A., Schleiss, A.J., Sumi, T., Murasaki, M., 2011. LSPIV implementation for environmental flow in various laboratory and field cases. J. Hydro Environ. Res. 5, 263–276. https://doi.org/10.1016/j.jher.2011.07.002.

Koutalakis, P., Zaimes, G.N., 2022. River flow measurements utilizing UAV-based surface velocimetry and bathymetry coupled with sonar. Hydrology 9, 148. https://doi.org/10.3390/hydrology9080148.

Kumar Vyas, J., Perumal, M., Moramarco, T., 2024. Non-contact discharge estimation at a river site by using only the maximum surface flow velocity. J. Hydrol. 638, 131505. https://doi.org/10.1016/j.jhydrol.2024.131505.

Lacaux, J.P., Tourre, Y.M., Vignolles, C., Ndione, J.A., Lafaye, M., 2007. Classification of ponds from high-spatial resolution remote sensing: application to Rift Valley fever epidemics in Senegal. Remote Sens. Environ. 106, 66–74. https://doi.org/10.1016/j.rse.2006.07.012.

Langat, P.K., Kumar, L., Koech, R., 2019. Monitoring river channel dynamics using remote sensing and GIS techniques. Geomorphology 325, 92–102. https://doi.org/10.1016/j.geomorph.2018.10.007.

Le Coz, J., Hauet, A., Pierrefeu, G., Dramais, G., Camenen, B., 2010. Performance of image-based velocimetry (LSPIV) applied to flash-flood discharge measurements in Mediterranean rivers. J. Hydrol. 394, 42–52. https://doi.org/10.1016/j.jhydrol.2010.05.049.

Le Coz, J., Renard, B., Vansuyt, V., Jodeau, M., Hauet, A., 2021. Estimating the uncertainty of video-based flow velocity and discharge measurements due to the conversion of field to image coordinates. Hydrol. Process. 35, e14169. https://doi.org/10.1002/hyp.14169.

Legleiter, C.J., 2023. Toolbox for River Velocimetry using Images from Aircraft (TRiVIA). https://doi.org/10.5066/P9AD3VT3.

Legleiter, C.J., Kinzel, P.J., 2024a. A framework to facilitate development and testing of image-based river velocimetry algorithms. Earth Surf. Proc. Landf. 49, 1361–1382. https://doi.org/10.1002/esp.5772.

Legleiter, C.J., Kinzel, P.J., 2024b. An enhanced and expanded toolbox for river velocimetry using images from aircraft (TRiVIA). River Res. Apps 40, 1602–1616. https://doi.org/10.1002/rra.4333.

Legleiter, C.J., Kinzel, P.J., 2023. The toolbox for river velocimetry using images from aircraft (TRiVIA). River Res. Apps. 39, 1457–1468. https://doi.org/10.1002/rra.4147.

Lewis, Q.W., Rhoads, B.L., 2018. LSPIV measurements of two-dimensional flow structure in streams using small unmanned aerial systems: 1. Accuracy assessment based on comparison with stationary camera platforms and in-stream velocity measurements. Water Resour. Res. 54, 8000–8018. https://doi.org/10.1029/2018WR022550.

Liu, W.-C., Lu, C.-H., Huang, W.-C., 2021. Large-scale particle image velocimetry to measure streamflow from videos recorded from unmanned aerial vehicle and fixed imaging system. Remote Sens. (Basel) 13, 2661. https://doi.org/10.3390/rs13142661.

Ljubičić, R., Dal Sasso, S.F., Zindović, B., 2024. SSIMS-flow: image velocimetry workbench for open-channel flow rate estimation. Environ. Model. Software 173, 105938. https://doi.org/10.1016/j.envsoft.2023.105938.

Ljubičić, R., Strelnikova, D., Perks, M.T., Eltner, A., Peña-Haro, S., Pizarro, A., Dal Sasso, S.F., Scherling, U., Vuono, P., Manfreda, S., 2021. A comparison of tools and techniques for stabilising unmanned aerial system (UAS) imagery for surface flow observations. Hydrol. Earth Syst. Sci. 25, 5105–5132. https://doi.org/10.5194/hess-25-5105-2021.

Manfreda, S., McCabe, M.F., Miller, P.E., Lucas, R., Pajuelo Madrigal, V., Mallinis, G., Ben Dor, E., Helman, D., Estes, L., Ciraolo, G., Müllerová, J., Tauro, F., De Lima, M.I., De Lima, J.L.M.P., Maltese, A., Frances, F., Caylor, K., Kohv, M., Perks, M., Ruiz-Pérez, G., Su, Z., Vico, G., Toth, B., 2018. On the use of unmanned aerial systems for environmental monitoring. Remote Sens. (Basel) 10, 641. https://doi.org/10.3390/rs10040641.

Manfreda, S., Miglino, D., Saddi, K.C., Jomaa, S., Eltner, A., Perks, M., Peña-Haro, S., Bogaard, T., Van Emmerik, T.H.M., Mariani, S., Maddock, I., Tauro, F., Grimaldi, S., Zeng, Y., Gonçalves, G., Strelnikova, D., Bussettini, M., Marchetti, G., Lastoria, B., Su, Z., Rode, M., 2024. Advancing river monitoring using image-based techniques: challenges and opportunities. Hydrol. Sci. J. 69, 657–677. https://doi.org/10.1080/02626667.2024.2333846.

McMahon, T.A., Peel, M.C., 2019. Uncertainty in stage–discharge rating curves: application to Australian Hydrologic Reference Stations data. Hydrol. Sci. J. 64, 255–275. https://doi.org/10.1080/02626667.2019.1577555.

Merkuryeva, G., Merkuryev, Y., Sokolov, B.V., Potryasaev, S., Zelentsov, V.A., Lektauers, A., 2015. Advanced river flood monitoring, modelling and forecasting. J. Comput. Sci. 10, 77–85. https://doi.org/10.1016/j.jocs.2014.10.004.

Meselhe, E.A., Peeva, T., Muste, M., 2004. Large scale particle image velocimetry for low velocity and shallow water flows. J. Hydraul. Eng. 130, 937–940. https://doi.org/10.1061/(ASCE)0733-9429(2004)130:9(937).

Mihel, A.M., Lerga, J., Krvavica, N., 2024. Estimating water levels and discharges in tidal rivers and estuaries: review of machine learning approaches. Environ. Model. Software 176, 106033. https://doi.org/10.1016/j.envsoft.2024.106033.

Mohajeri, S.H., Noori, A., Mehraein, M., Nabipour, M., 2024. On the performance of streamflow gauging using CCTV-integrated LSPIV in diverse hydro-environmental conditions. Environ. Monit. Assess. 196, 202. https://doi.org/10.1007/s10661-024-12369-9.

Munawar, H.S., Hammad, A.W.A., Waller, S.T., 2022. Remote sensing methods for flood prediction: a review. Sensors 22, 960. https://doi.org/10.3390/s22030960.

Muste, M., Fujita, I., Hauet, A., 2008. Large-scale particle image velocimetry for measurements in riverine environments. Water Resour. Res. 44, 2008WR006950. https://doi.org/10.1029/2008WR006950.

Muste, M., Hoitink, T., 2017. Measuring flood discharge. Oxford Research Encyclopedia of Natural Hazard Science. Oxford University Press https://doi.org/10.1093/acrefore/9780199389407.013.121.

Peña-Haro, S., Carrel, M., Lüthi, B., Hansen, I., Lukes, R., 2021. Robust Image-based streamflow measurements for real-time continuous monitoring. Front. Water 3, 766918. https://doi.org/10.3389/frwa.2021.766918.

Perks, M.T., 2020. KLT-IV v1.0: image velocimetry software for use with fixed and mobile platforms. Geosci. Model Dev. 13, 6111–6130. https://doi.org/10.5194/gmd-13-6111-2020.

Piégay, H., Arnaud, F., Belletti, B., Bertrand, M., Bizzi, S., Carbonneau, P., Dufour, S., Liébault, F., Ruiz-Villanueva, V., Slater, L., 2020. Remotely sensed rivers in the Anthropocene: state of the art and prospects. Earth Surf. Proc. Landf. 45, 157–188. https://doi.org/10.1002/esp.4787.

Pizarro, A., Dal Sasso, S.F., Manfreda, S., 2020a. Refining image-velocimetry performances for streamflow monitoring: seeding metrics to errors minimization. Hydrol. Process. 34, 5167–5175. https://doi.org/10.1002/hyp.13919.

Pizarro, A., Dal Sasso, S.F., Perks, M.T., Manfreda, S., 2020b. Identifying the optimal spatial distribution of tracers for optical sensing of stream surface flow. Hydrol. Earth Syst. Sci. 24, 5173–5185. https://doi.org/10.5194/hess-24-5173-2020.

Pumo, D., Alongi, F., Ciraolo, G., Noto, L., 2021. Optical methods for river monitoring: a simulation-based approach to explore optimal experimental setup for LSPIV. Water 13, 247. https://doi.org/10.3390/w13030247.

Pumo, D., Alongi, F., Nasello, C., Noto, L.V., 2025. A simplified method for estimating the alpha coefficient in surface velocity based river discharge measurements. J. Hydrol. 648, 132468. https://doi.org/10.1016/j.jhydrol.2024.132468.

Ran, Q., Li, W., Liao, Q., Tang, H., Wang, M., 2016. Application of an automated LSPIV system in a mountainous stream for continuous flood flow measurements. Hydrol. Process. 30, 3014–3029. https://doi.org/10.1002/hyp.10836.

Rawat, K.S., Sahu, S.R., Singh, S.K., Chander, S., Gujrati, A., 2023. Water quality analysis using normalized difference chlorophyll index (NDCI) and normalized difference turbidity index (NDTI), using Google earth engine platform. In: 2023 International Conference on Modeling, Simulation & Intelligent Computing (MoSICom). Presented at the 2023 International Conference on Modeling, Simulation & Intelligent Computing (MoSICom), pp. 408–413, 10.1109/MoSICom59118.2023.10458842.

Rosero Legarda, J.A., Argoti Santacruz, A.N., Mafla Chamorro, F.R., 2022. River velocity through LSPTV technique using UAVs. Rev. Ing. Univ. Medellin 21, 1–17. https://doi.org/10.22395/rium.v21n41a5.

Shanafield, M., Bourke, S.A., Zimmer, M.A., Costigan, K.H., 2021. An overview of the hydrology of non-perennial rivers and streams. WIREs Water 8, e1504.

Singh, R., Saritha, V., Pande, C.B., 2024. Monitoring of wetland turbidity using multi-temporal Landsat-8 and Landsat-9 satellite imagery in the Bisalpur wetland, Rajasthan, India. Environ. Res. 241, 117638. https://doi.org/10.1016/j.envres.2023.117638.

Sivapragasam, C., Muttil, N., 2005. Discharge rating curve extension – a new approach. Water Resour. Manag. 19, 505–520. https://doi.org/10.1007/s11269-005-6811-2.

Smart, G.M., 1992. Stage-discharge discontinuity in composite flood channels. J. Hydraul. Res. 30, 817–833. https://doi.org/10.1080/00221689209498912.

Strelnikova, D., Perks, M.T., Dal Sasso, S.F., Pizarro, A., 2023. River flow monitoring with unmanned aerial system. In: Unmanned Aerial Systems for Monitoring Soil, Vegetation, and Riverine Environments. Elsevier, pp. 231–269 https://doi.org/10.1016/B978-0-323-85283-8.00012-6.

Tang, H., Chen, C., Chen, H., Huang, J., 2008. An improved PTV system for large-scale physical river model. J. Hydrodyn. 20, 669–678. https://doi.org/10.1016/S1001-6058(09)60001-9.

Tauro, F., Piscopia, R., Grimaldi, S., 2019. PTV-stream: a simplified particle tracking velocimetry framework for stream surface flow monitoring. Catena 172, 378–386. https://doi.org/10.1016/j.catena.2018.09.009.

Tauro, F., Selker, J., Van De Giesen, N., Abrate, T., Uijlenhoet, R., Porfiri, M., Manfreda, S., Caylor, K., Moramarco, T., Benveniste, J., Ciraolo, G., Estes, L., Domeneghetti, A., Perks, M.T., Corbari, C., Rabiei, E., Ravazzani, G., Bogena, H., Harfouche, A., Brocca, L., Maltese, A., Wickert, A., Tarpanelli, A., Good, S., Lopez Alcala, J.M., Petroselli, A., Cudennec, C., Blume, T., Hut, R., Grimaldi, S., 2018. Measurements and observations in the XXI century (MOXXI): innovation and multi-disciplinarity to sense the hydrological cycle. Hydrol. Sci. J. 63, 169–196. https://doi.org/10.1080/02626667.2017.1420191.

Thielicke, W., Stamhuis, E.J., 2014. PIVlab – towards user-friendly, affordable and accurate digital particle image velocimetry in MATLAB. J. Open Res. Softw. 2. https://doi.org/10.5334/jors.bl.

Watanabe, K., Fujita, I., Iguchi, M., Hasegawa, M., 2021. Improving accuracy and robustness of space-time image velocimetry (STIV) with deep learning. Water 13, 2079. https://doi.org/10.3390/w13152079.

Wei, Z., Jia, K., Liu, P., Jia, X., Xie, Y., Jiang, Z., 2021. Large-scale river mapping using contrastive learning and multi-source satellite imagery. Remote Sens. (Basel) 13, 2893. https://doi.org/10.3390/rs13152893.

Wijaya, F., Liu, W.-C., Suharyanto, Huang, W.-C., 2023. Comparative assessment of different image velocimetry techniques for measuring river velocities using unmanned aerial vehicle imagery. Water 15, 3941. https://doi.org/10.3390/w15223941.

Willmott, C.J., Robeson, S.M., Matsuura, K., 2012. A refined index of model performance. Intl. J. Climatol. 32, 2088–2094. https://doi.org/10.1002/joc.2419.

Winsemius, H.C., Van Beek, L.P.H., Jongman, B., Ward, P.J., Bouwman, A., 2013. A framework for global river flood risk assessments. Hydrol. Earth Syst. Sci. 17, 1871–1892. https://doi.org/10.5194/hess-17-1871-2013.

Xu, M., Liu, H., Mitchell, D., Lu, Y., Beck, R., Cohen, S., Shu, S., Dimova, N., 2023. Mapping river turbidity at a large basin-scale with a spatially transferable ensemble model using Landsat 8 multispectral imagery. Int. J. Remote Sens. 44, 4486–4505. https://doi.org/10.1080/01431161.2023.2237663.

Yan, Y., Wang, Y., Yu, C., Zhang, Z., 2023. Multispectral remote sensing for estimating water quality parameters: a comparative study of inversion methods using unmanned aerial vehicles (UAVs). Sustainability 15, 10298. https://doi.org/10.3390/su151310298.

Zhang, Z., Wang, X., Fan, T., Xu, L., 2013. River surface target enhancement and background suppression for unseeded LSPIV. Flow Meas. Instrum. 30, 99–111. https://doi.org/10.1016/j.flowmeasinst.2012.12.002.

Zhao, Z., Li, H., Song, X., Sun, W., 2023. Dynamic monitoring of surface water bodies and their influencing factors in the yellow river basin. Remote Sens. (Basel) 15, 5157. https://doi.org/10.3390/rs15215157.